AFRL-AFOSR-JP-TR-2017-0022

Flexible 2D RF Nanoelectronics based on Layered Semiconductor Transistor (NBIT III)

Costas Grigoropoulos
UNIVERSITY OF CALIFORNIA BERKELEY

11/11/2016
Final Report

Air Force Research Laboratory
AF Office Of Scientific Research (AFOSR)/ IOA
Arlington, Virginia 22203
Air Force Materiel Command

REPORT DOCUMENTATION PAGE

Form Approved
OMB No. 0704-0188

1. REPORT DATE *(DD-MM-YYYY)*	2. REPORT TYPE	3. DATES COVERED *(From - To)*
07-03-2017	Final	14 Aug 2013 to 13 Aug 2016

4. TITLE AND SUBTITLE
Flexible 2D RF Nanoelectronics based on Layered Semiconductor Transistor (NBIT III)

5a. CONTRACT NUMBER

5b. GRANT NUMBER
FA2386-13-1-4123

5c. PROGRAM ELEMENT NUMBER
61102F

6. AUTHOR(S)
Costas Grigoropoulos

5d. PROJECT NUMBER

5e. TASK NUMBER

5f. WORK UNIT NUMBER

7. PERFORMING ORGANIZATION NAME(S) AND ADDRESS(ES)
UNIVERSITY OF CALIFORNIA BERKELEY
200 CALIFORNIA HALL #1500
BERKELEY, CA 947201502 US

8. PERFORMING ORGANIZATION REPORT NUMBER

9. SPONSORING/MONITORING AGENCY NAME(S) AND ADDRESS(ES)
AOARD
UNIT 45002
APO AP 96338-5002

10. SPONSOR/MONITOR'S ACRONYM(S)
AFRL/AFOSR IOA

11. SPONSOR/MONITOR'S REPORT NUMBER(S)
AFRL-AFOSR-JP-TR-2017-0022

12. DISTRIBUTION/AVAILABILITY STATEMENT
A DISTRIBUTION UNLIMITED: PB Public Release

13. SUPPLEMENTARY NOTES

14. ABSTRACT
Experimental and computational studies in multidisciplinary fields of electrical, mechanical engineering, and materials science were conducted to achieve the following major goals of this project: Development of laser annealing for improving contact quality to achieve high-performance devices on a flexible platform Modification of optical and electrical properties of 2D materials with laser assisted and site selective doping and alloying Development of plasmonic laser welding process and solution based embedded polyimide (PI) structure for making highly robust flexible/wearable devices Stress-strain analysis for optimizing the structure design (e.g. radius of curvature, thickness of the structure, etc.) Large-area and highly crystalline CVD-grown 2D films Optimization of device designs to achieve flexible biosensors with 2D materials for highly sensitive and selective biological detection Through the project, aforementioned results demonstrate that pulsed laser process is an attractive technology for realizing high performance flexible MoS2 TFTs in analog/digital integrated circuits; they are published in peer-reviewed journals (more than 17 papers) and are presented at conferences (more than 10 times). In addition, we are continuing our research on flexible/wearable electronics and their applications, especially for sensors.

15. SUBJECT TERMS
NBIT, Nanoscience, AOARD

16. SECURITY CLASSIFICATION OF:			17. LIMITATION OF ABSTRACT	18. NUMBER OF PAGES	19a. NAME OF RESPONSIBLE PERSON
a. REPORT	b. ABSTRACT	c. THIS PAGE			SERNA, MARIO
Unclassified	Unclassified	Unclassified	SAR	33	19b. TELEPHONE NUMBER *(Include area code)* 315-227-7002

Standard Form 298 (Rev. 8/98)
Prescribed by ANSI Std. Z39.18

NBIT Final Report for AOARD Grant FA2386-13-1-4123

"**Flexible 2D Nanoelectronics based on Layered Semiconductor Transistor (NBIT III)**"

November. 10. 2016

Name of Principal Investigators (PI, US): Prof. Costas P. Grigoropoulos
- e-mail address : cgrigoro@berkeley.edu
- Institution : University of California, Berkeley
- Mailing Address : 6129 Etcheverry Hall, Berkeley, CA 94720-1740, USA
- Phone : +1-510-642-2525
- Fax : +1-510-642-5539

Name of Principal Investigators (Co-Pis, KOR): Prof. Sunkook Kim
- e-mail address : seonkuk@khu.ac.kr
- Institution : Kyung Hee University
- Mailing Address : 1 Seocheon-dong, Giheung-gu, Yonginsi, Gyeonggi-do 446-701, South Korea
- Phone : +82-01-5038-9497
- Fax : N/A

Name of Principal Investigators (Collaborator, KOR): Prof. Woong Choi
- e-mail address : woongchoi@kookmin.ac.kr
- Institution : Kookmin University
- Mailing Address : 77 Jeongneung-Ro, Seongbuk-gu, Seoul 136-702, South Korea Phone : +82-2-910-4229
- Fax : N/A

Period of Performance: 08/19/2013 – 08/13/2016

Abstract: Laser enables the achievement of superb interfacial characteristics between electrode and semiconducting material contact surface and is also useful for a reduction in contact resistance. The irradiation of a pulsed laser with high energy density and short wavelength onto the electrodes leads to the thermal annealing effect at the locally confined small area that needs high temperature without extreme thermal damage. Unlike pulsed laser annealing, conventional thermal annealing affects the entire panel including unwanted areas where the annealing process should be excluded.

2D transition metal dichalcogenides (TMDCs) with the formula of MX_2 (M = Mo, W; X = S, Se, Te) composed of vertically stacked layers held together by van der Waals interactions, have shown potential to complement or overcome drawbacks of conventional opto- and electronic device applications (e.g. transistors, photodetectors, electroluminescent devices and sensors), because of their unique optical and electrical properties: relatively large bandgap (1.2-1.9 eV), high mobility at room temperature (up to ~500 $cm^2V^{-1}s^{-1}$), low subthreshold swing (SS, ~70 mV $decade^{-1}$), high on/off ratios (~10^7), and potential amenability to low-cost fabrication sequence. Tuning their properties by modulating the free carrier type and density and composition can offer an exciting new pathway to various practical nanoscale electronics. However, there are several key challenges that lie ahead before the transistors based on 2D layered semiconductors can be integrated into flexible/stretchable circuits. The main issues include instability of flexible structures with respect to various mechanical stresses, inaccessibility of large area growth/coverage of layered semiconductors, and tunability of TMDC-based layered semiconductors for ultra-sensitive sensors of high specificity. These challenges give rise to the focus areas defined in our research plan for this project.

Experimental and computational studies in multidisciplinary fields of electrical, mechanical engineering, and materials science were conducted to achieve the following major goals of this project:

- Development of laser annealing for improving contact quality to achieve high-performance devices on a flexible platform
- Modification of optical and electrical properties of 2D materials with laser assisted and site selective doping and alloying
- Development of plasmonic laser welding process and solution based embedded polyimide (PI) structure for making highly robust flexible/wearable devices
- Stress-strain analysis for optimizing the structure design (e.g. radius of curvature, thickness of the structure, etc.)
- Large-area and highly crystalline CVD-grown 2D films
- Optimization of device designs to achieve flexible biosensors with 2D materials for highly sensitive and selective biological detection

Through the project, aforementioned results demonstrate that pulsed laser process is an attractive technology for realizing high performance flexible MoS_2 TFTs in analog/digital integrated circuits; they are published in peer-reviewed journals (more than 17 papers) and are presented at conferences (more than 10 times). In addition, we are continuing our research on flexible/wearable electronics and their applications, especially for sensors.

Introduction: Flexible and stretchable electronics represent a critical frontier in the transformation of rigid, table-top micro/nano electronics into portable, wearable systems that can be integrated into a variety of emerging technologies from sensing and monitoring to human-inspired applications. Many conventional structures, materials, and processes are not compatible with flexible/stretchable device layouts. These requirements pose significant challenges that require a new, adaptive paradigm for the low-thermal budget (< 100 °C) and functional components on a lightweight and inexpensive flexible platform. Thin-film transistors (TFTs) are representative applications in the field of flexible/stretchable electronics. Currently, users require new and more advanced displays for mobile phones, portable devices, and even televisions, with features including ultra-high resolution, higher frame rates (high driving speed), low power consumption, and larger size. For realizing high performance of TFTs, we should consider metal-semiconductor junctions that are indispensable to the structure of TFTs, because non-ideal electric contacts can form Schottky barriers at the junctions, and the undesirable contacts can hamper the inherent electrical characteristics of MoS_2. Therefore, to reduce the contact resistance (R_c) and Schottky barrier, various efforts (doping, the use of scandium metal with a low work function, and thermal annealing) have been reported. However, there are challenges and limitations to moving forward in flexible electronics technologies. The chemical doping effect is gradually reduced over time. Moreover, scandium metals have been classified as a rare earth element and difficulties have been encountered in preparing them. The typically used flexible substrates (e.g. poly(ethylene naphthalate) (PEN), poly(ethylene terephthalate) (PET), and polyimide (PI)), have a low thermal budget (< 200 °C). Therefore, high thermal annealing processes could lead to deformation in plastic substrates.

Unlike conventional thermal annealing, which affects the entire panel including unwanted areas where the annealing process should be excluded, the irradiation of a pulsed laser with high energy density and short wavelength onto a metal electrode leads to the thermal annealing effect in a small, locally confined area that requires high temperature without extreme thermal damage. Also, a laser enables the achievement of superb interfacial characteristics between metal and semiconducting material contact surfaces, resulting in reduced R_c and improved interfacial morphology. Numerical thermal simulation for the temperature distribution, transmission electron microscopy (TEM) analysis, current-voltage measurements, and contact-free mobility extracted from the Y-function method (YFM) enable understanding of the compatibility and the effects of pulsed laser annealing process; the enhanced performance originated not only from a decrease in the Schottky barrier effect at the contact, but also an improvement of the channel interface.

In addition, doping is simple and versatile methods to accomplish our goal. However, previous efforts have mostly focused on doping TMDCs by means of charge transfer from adsorbed molecules, electrostatic or physisorption gating, defect engineering, and substitutional doping during the growth. These methods result in uniform doping or composition without spatial resolution. However, for nanoscale devices using ultrathin TMDCs as an ultra-thin body, to minimize random dopant fluctuation, ensure device performance reproducibility, and scale down the device size and scale up device functionalities, site-specific doping with precise carrier/composition level control becomes essential. Here we provide a systematic approach to this problem, demonstrating superior, in-situ control of the spatial distribution and doping level of TMDCs. Our laser induced doping process is spatially local and selective, and the doping level is widely tunable by varying the duration and intensity of laser irradiation. Moreover, laser doping can be digitally controlled and is an air-stable process of TMDCs for high-quality, high-fidelity nanodevices.

Many research groups have attempted to develop alternative conductive flexible electrodes, since the usual metal films are rather ductile and require expensive vacuum

deposition techniques. Candidate electrode systems that have been studied and introduced up to date include highly conductive poly(3,4- ethylenedioxythiophene):poly(4-styrenesulfonate), metal grids, graphene, carbon nanotubes, nanotube– polymer composites, and silver nanowire (Ag NW) meshes. Among the suggested materials, 2D random networks of Ag NWs are promising because of their compatibility with cost-effective solution processes and the reasonably high electrical conductivity. However, random network of Ag NWs may be inappropriate for practical applications. First, the electrical properties must be preserved upon mechanical bending or stretching. Next, the surface roughness of the entire electrode layer must be sufficiently small in order to guarantee fast carrier transport along the overlaying active layers. Finally, the NWs must adhere well to the substrate and form contacts at their intersections. The electrical contact at the Ag NW junctions can be improved by laser welding, which is based on highly localized heating induced by plasmonic effects.

Experiment:

a. Laser annealing

Fig. 1(a) shows the schematic architecture of our flexible multilayer MoS_2 FETs on the PEN substrate (DuPont Teijin Films, USA).

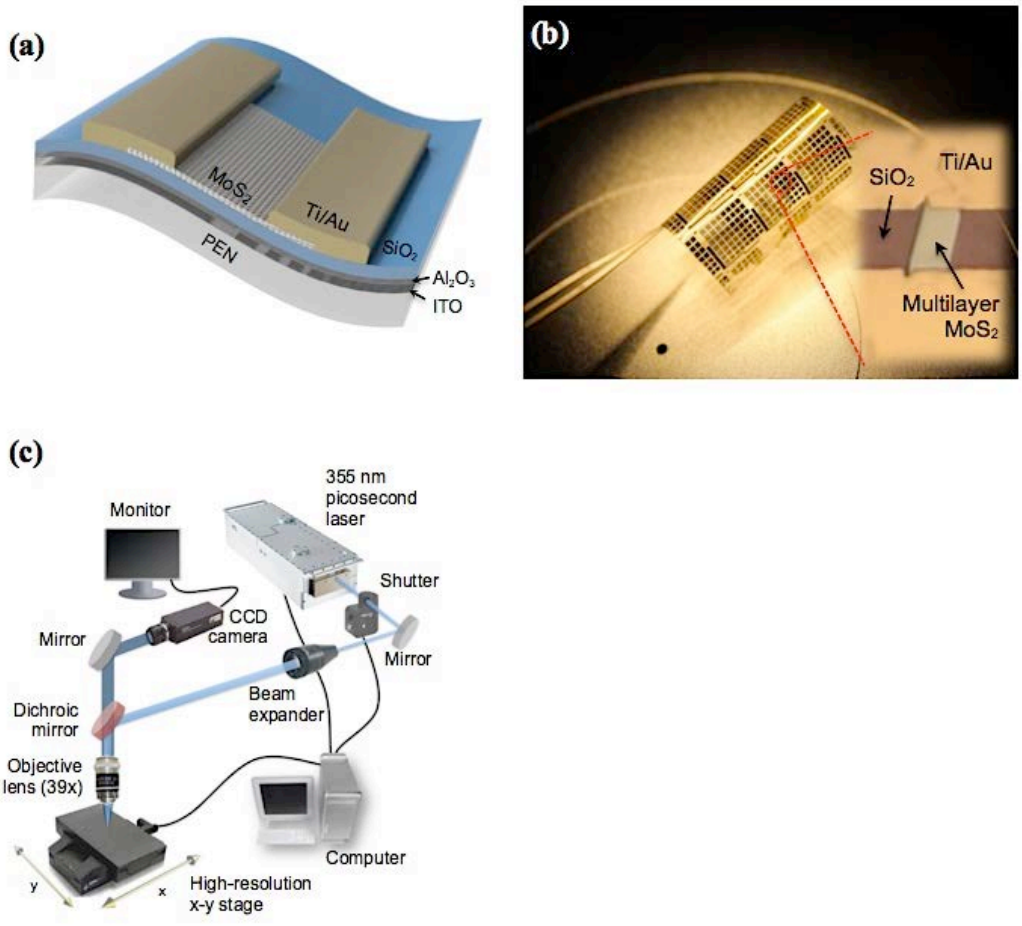

Figure 1: Flexible multilayer MoS_2 FETs and pulsed laser annealing system. (a) Cross-sectional schematic structure of multilayer MoS_2 FETs with a 300-nm-thick SiO_2 gate dielectric. Picosecond laser irradiation with a Gaussian beam profile is focused and scanned along the edge of the source and drain electrodes. (b) Top-view of the optical microscope image for multilayer MoS_2 FETs after fabricating completely. (c) Schematic view of the optical setup for picosecond laser annealing.

For a bottom gate electrode, a 100-nm-thick indium thin oxide (ITO) was deposited on the PEN substrate at room temperature. Then, dual films (atomic-layer-deposited (ALD) Al_2O_3 of 50 nm / sputter-deposited SiO_2 of 250 nm) were formed as a gate dielectric layer. A MoS_2 flake with a thickness of ~ 50 nm was mechanically transferred from bulk MoS_2 crystals (SPI Supplies, USA) on the deposited dielectric layer. After that, Ti (10 nm) and Au (300 nm) were continuously deposited by electron-beam evaporation at room temperature. Finally, conventional UV photolithography and lift-off techniques allowed definition of the source and drain electrodes. Fig. 1(b) shows a proof-of-concept realization of a completely fabricated flexible multilayer MoS_2 FET rolled up in a curved shape and an optical microscope (BX60, Olympus) image of the top of the device (Fig. 1b inset). A yttrium vanadate (Nd:YVO_4) picosecond pulsed laser (Newport Corp., USA) having a wavelength of 355 nm, a pulse width based on full width at half maximum of 12 ps, and a pulse repetition rate of 80 MHz was applied for selectively focused annealing at the contact regions. Note that the shape of the pulsed laser beam was Gaussian with a 1.5-μm beam diameter at a $1/e^2$ peak irradiance, and was obtained through a 39× objective lens with a numerical aperture (NA) of 0.5. Moreover, a computer simultaneously operated laser power, scan speed, position of the high-resolution x-y positioning stage (Aerotech, USA), and optical shutter during the annealing process, as shown in Fig. 1(c).

Additionally, the Korean partner fabricated TFTs based on multilayer MoS_2 using mechanically exfoliated multilayer MoS_2 flakes on a highly-doped p-type Si wafer with a thermally grown SiO_2 layer (300 nm). Electrical contacts (100 μm × 100 μm) were patterned on top of MoS_2 flakes using conventional photolithography and lift-off techniques. Ti (100 nm) was deposited by electron-beam evaporation at room temperature. The device was then annealed at 400°C in a vacuum tube furnace for 2 hours (100 sccm Ar and 10 sccm H_2). The thickness of MoS_2 channels measured by atomic force microscope (AFM; Park Systems, XE-100) was in the range of 20-80 nm. Electrical characterizations were carried out with I-V measurements (Keithley, Semiconductor Characterization System 4200-SCS) in vacuum.

b. Laser doping

The schematic diagram of the laser-assisted doping method shows in Fig. 2. The laser serves two major functions in this doping method, one is to create surface vacancies in the TMDC materials and the other is to dissociate the dopant gas, releasing the dopant molecules to incorporate into the vacancy sites. The phosphine (PH_3) was introduced as p-type dopant precursor for ultrathin-layered materials, in contrast to its use for n-type doping silicon. The PH_3/Si system has been extensively studied both experimentally and through theoretical modeling. On the basis of this insight, and despite the structural difference between silicon and TMDCs, it is possible to adopt the vacancy mechanism in this work. In terms of vacancy formation, it is noted that laser power just below dissociation of the TMDC materials, is enough for breaking the PH_3 (its dissociation temperature is 685 K) since the TMDC material dissociation temperature is in the range of 1200~1400 K.

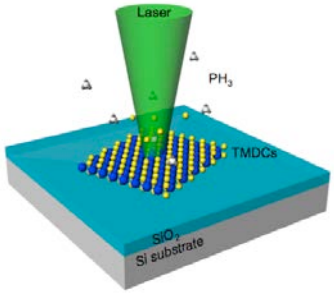

Figure 2: Schematic diagram of the laser assisted doping method. A mechanically exfoliated MoS_2 flake is transferred onto the 300nm SiO_2 on Si substrate and Phosphine (PH_3) as a dopant gas

c. Laser welding

To make a Ag NWs network, a vacuum transfer method was applied because the vacuum suction pressure can distribute the normal force uniformly on the substrate. Firstly, a Teflon filter (SterliTech, 0.2 μm pore size and 47 mm in diameter) was placed at the neck of a side arm flask connected to a vacuum pump and the glass cap was put on the Teflon filter for filtration. Then, 25 μL of Ag NW solution (Seashell Technology, with 25 ± 10 μm length and 30 ± 10 nm diameter) dispersed in sufficient isopropyl alcohol (as a carrier fluid) was poured into the cap. Note that Ag concentration was around 5.3 mg mL^{-1}. Only Ag NWs were filtered on the Teflon filter. After drying for 3 hours, the filtered Ag NWs were directly transferred from the filter to the target substrate (Glass-1 in Fig. 3) with a uniform normal pressure for 1−2 hours. Owing to very low surface energy of Teflon, most of Ag NWs were transferred easily and a uniform 2D Ag NWs percolation network was formed on the target substrate. The as-prepared Ag NWs had physical contacts, which is susceptible to the shear force and can result in high contact resistance. Therefore, to enhance the electrical property by forming good contacts, a laser beam with 532 nm wavelength (Solo I Nd:YAG, New Wave) was irradiated onto the Ag NWs network. Also, through an objective lens, the effective area was scaled up to ~cm scale by an out-of-focal-plane process with a maximum laser energy of 20 mJ.

For a flexible substrate, PI solution was spin-coated on the surface of the laser-welded Ag NWs at 3,000 rpm for 30 s and thermally solidified at 60 °C for 30 min. The Ag NWs-embedded PI layer was mechanically detached from the Glass-1, and attached on the carrier substrate (Glass-2) upside down with 3M tapes at each corner. The organic GI was formed by spin-coating SU-8 2000.5 (Microchem®) onto the Ag NWs gate electrode (3,000 rpm for 30 s), followed by baking at 110 °C for 5 min and 130 °C for 5 min. Then, a 30-nm-thick amorphous Al_2O_3 was deposited by ALD (Lucida D100, South Korea) with trimethylaluminum as an Al precursor and H_2O as an oxidant. Mechanically exfoliated multilayered MoS_2 flakes were transferred onto the Al_2O_3 film. After E-beam evaporation of a Ti/Au (20/100 nm) layer, source (drain) electrodes were fabricated by conventional photolithography and etching techniques. The as-fabricated multilayer MoS_2 TFTs on flexible PI substrate was post-annealed at 150 °C for 2 hours in vacuum oven ($\leq 10^{-3}$ torr) in order to reduce contact resistance between the active layer and the S/D electrodes. Transparent PET film with a thickness of 100 μm, as a protective as well as supportive layer for the flexible MoS_2 TFTs, was laminated beneath the PI layer with the aid of an acrylate resin-based pressure sensitive adhesive after the separation of the flexible MoS_2 TFTs from the carrier substrate.

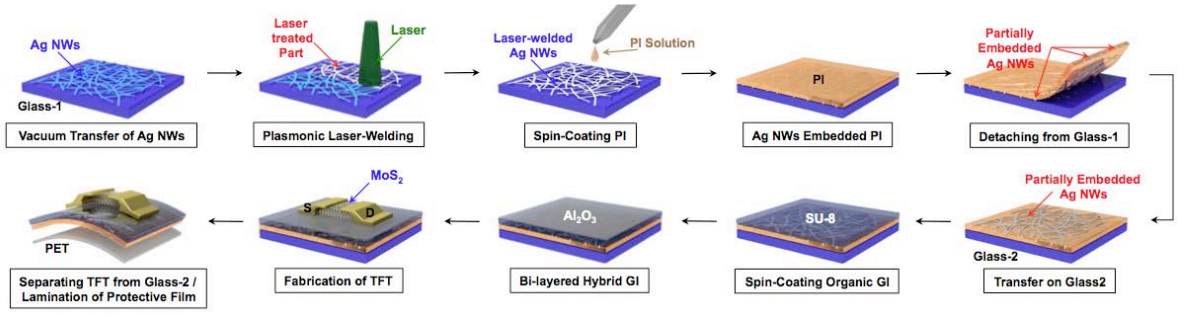

Figure 3: Flexible multilayer MoS_2 TFTs. Schematic flow chart of the fabrication procedure consisting of the laser welded/embedded 2D Ag NWs network, solution-based thin PI, and organic/inorganic hybrid GI for a highly flexible TFT platform.

Results and Discussion:

a. Laser annealing

i. Thermal analysis for pulsed laser annealing system

Profound understanding of ultrashort laser pulse induced temperature field requires detailed knowledge of the fundamental interactions between laser light (photons) and matter (electron and phonon systems). In metals, initially electrons primarily absorb the laser photon energy. In the Au film with the thickness of 400 nm, the optical absorption depth is about 16.3 nm. The electron system temperature rises instantaneously in response to the applied photon flux. Thermalized hot electrons diffuse into the material and transfer their energy to the lattice (within 10^{-12} ~ 10^{-10} s) until the electron and lattice temperatures equilibrate through electron-phonon coupling. This equilibration occurs within the pulse for pulse lengths in the range 10 to 60 ps. In the gold system, this thermal equilibrium time of the electron and lattice is about 40 ps. Therefore, the temperatures of electron and lattice are different during the single pulse duration (12 ps) applied in our experiment. Consequently, the hot electron diffusion length is deeper than both the optical absorption depth and the heat diffusion length $\delta \sim \sqrt{4\alpha dt}$ (where δ is the depth of heat penetration, α is the diffusivity of materials, and *dt* is the pulse duration). In order to obtain a more accurate predictive solution, the two-temperature model (TTM) could be applied in this transient non-equilibrium case. However, the TTM model that is by itself an approximation of the Boltzmann transport equation has been widely used to understand the origin of ultrashort electron dynamics under single laser pulse excitation of width 10^{-15} ~ 10^{-12} s. Prediction of the transient temperature distribution induced by high repetition rate pulsed laser over a long time scale as in our system by using the TTM poses a significant challenge due to the required prohibitively long computing time. In our 80 MHz repetition rate case, we have to compute the TTM system of equations over 80,000,000 pulses in order to analyze only one second. Although the amplitude of the ps duration temperature spikes would be smaller by the TTM model, the heat accumulation that is driven by thermal diffusion would not differ from the presented thermal model prediction.

For a picosecond pulsed laser source applied under our experimental conditions, we investigated temperature distribution during laser annealing process by 3-dimensional (3D) finite-difference methods (FDM) using COMSOL Multiphysics. The equilibrium temperature approximation is adopted since it reduces the required computational cost. As previously noted, the assumption of equilibrium temperature would overestimate the transient temperature. However, the approximate thermal solution shows good agreement with the results of real laser damage test. To calculate the approximated temperature distribution inside laser-heated Au electrode, the following heat flow equation is used:

$$\rho C_p \frac{\partial T}{\partial t} = \nabla(k(T)\nabla T) + Q(x,y,z) \qquad (1)$$

where ρ is the density, C_p is the specific heat, k is the thermal conductivity, and Q is the heat source term. In the volumetric heating with a Gaussian laser beam case, the heat source term is expressed as:

$$Q(x,y,z) = Q_0 (1\text{-}R_c) \frac{A_c}{2\pi\sigma_x\sigma_y} e^{-\left[\frac{(x-x_0)^2}{2\sigma_x^2}+\frac{(y-y_0)^2}{2\sigma_y^2}\right]} . e^{-A_c z} \qquad (2)$$

where Q_0, R_c, A_c, and $\sigma_{x,y}$ indicate the total input power, the reflection coefficient, the absorption coefficient, and pulse *x,y* standard deviation, respectively. Note that, for the accuracy of the analysis, temperature dependent thermophysical properties of Au electrode used as absorption layer were applied. However, other material properties,

R_c and A_c, are assumed to be constants. In addition, the thermal properties of multilayer MoS_2 were included in this analysis by using the experimental values.

The top surface of Au electrode is aligned with z = 0 and the Gaussian laser beam moves over the surface at a specific speed, 10 μm s^{-1} along a prescribed path (Fig. 4(a)) because charge injection mainly occurs from the edge of the metal electrodes into the semiconducting channels. In addition, the temperature generated by the laser annealing did not cool down to below ambient temperature before the next pulse arrives due to the high repetition rate (80 MHz). This heat accumulation effect can induce changes in the characteristics of MoS_2 FETs and have made a pulsed laser usable for annealing flexible electronics. Fig. 4(b) shows the optical images of laser-irradiated Au contacts on plastic substrate. The laser power over 40 mW severely damaged the Au electrode because generated heat could exceed the melting temperature of Au (1330 K). To predict the generated heat and temperature distribution inside the sample, we computed the temperature with respect to the scanned time at particular points. Note that we calculate the temperature distribution for average laser powers of 18.3 mW (orange region) and 43.0 mW (blue region); 18.3mW makes the best reduction of contact resistance and 43.0 mW is the initial power of damage based on real experimental results (Fig. 4(b)). While the moving pulsed laser beam with the speed of 10 μm s^{-1} directly irradiated on the Au surface, the effect of the high frequency transients by an ultrashort pulsed laser lasted till the time of 0.2 s; the temperature distribution then consists of high-frequency and picosecond-duration spikes superposed on a continuous base as shown in the inset of Fig. 4(c). In agreement with the real test of laser irradiation (Fig. 4(b)), for the laser power of 43.0 mW, the temperature exceeded the melting point of Au (1330 K) as indicated by the orange region in Fig. 4(c). Such a high temperature may inflict thermal damage on the Au contacts. However, the induced temperature by the laser power of 18.3 mW is 533 K (blue region in Fig. 4(c)). This is a comparable temperature with those of thermal annealing used in previous studies to improve device performance, as well as with our experimental results detailed in subsequent sections. Also, generated heat by laser absorption at the top surface could affect the interfaces by heat conduction as well as the contact. Therefore, we expand thermal analysis into the interfaces. Note that interested interfaces are between channel and dielectric layer (point 2) and between dielectric and substrate layer (point 3) in Fig 4(d). In Fig. 4(c), we already analyzed point 1. As shown in Fig 4(d), at point 2, the reached heat around 480 K (~210 °C) is not low to ignore because the induced temperature is high enough for thermal annealing, according to other reports.

Unfortunately, we cannot obtain the result measured directly to confirm the effect on the interfaces. However, we've tried to verify the impact on the interfaces indirectly through the new approach, YFM (see the next session). Point 3 shows that the reached heat, 365 K (~90 °C) can be below the thermal resistance of PEN substrate (~170 °C). Therefore, we can know and expect that there is no thermal damage after laser process. We already proved it through the laser experiment (Fig 4(b)).

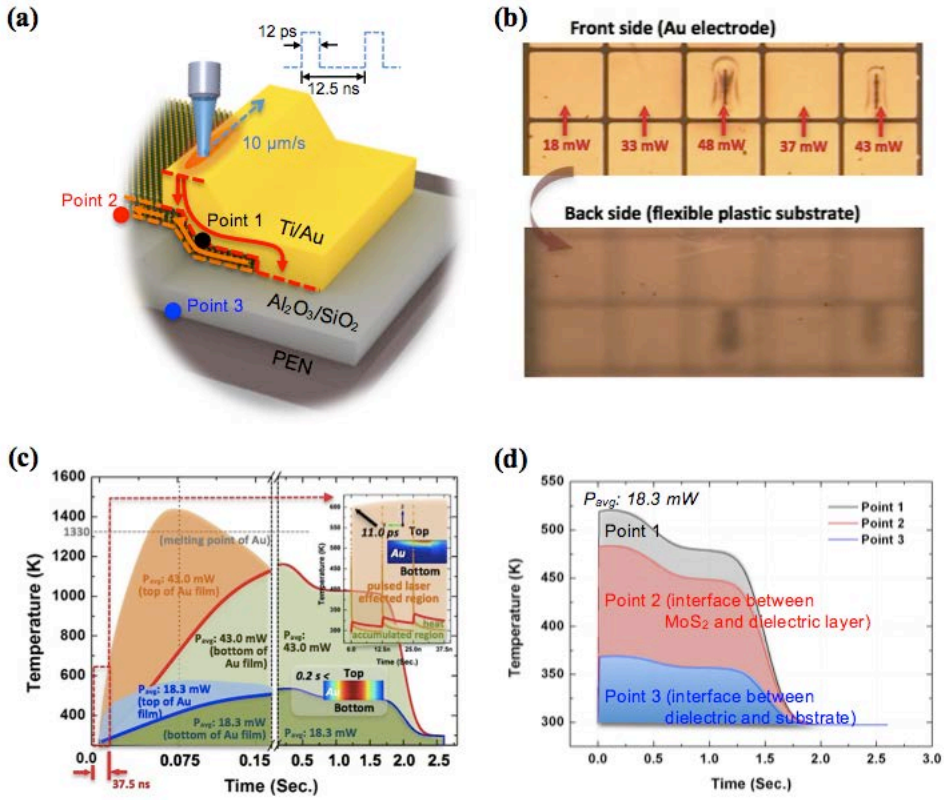

Figure 4: Numerical thermal analysis of temperature distribution under a moving picosecond-pulsed laser source. (a) Spatial schematic images of laser-irradiated Au contacts at a speed of 10 μm/s on a flexible PEN substrate and three points of interest: point 1 (the interface between the contact and MoS_2), point 2 (the interface between MoS_2 and the dielectric layer), and point 3 (the interface between the dielectric layer and the substrate). (b) the optical images of the front and back side of laser-irradiated Au contacts on a flexible plastic substrate. Au contacts irradiated with laser power > 40 mW show severe damage. (c, d) predicted temperature distributions versus exposure time at the three specific points when a picosecond pulsed laser was applied and scanned onto the top surface (Au) at ambient conditions.

ii. TEM analysis: Schottky barrier at contacts

Fig. 5 shows the cross-sectional TEM image. Through the TEM images before and after laser annealing, there are several possible explanations for the effects of laser process on the flexible multilayer MoS_2 FET. The first possibility is removing unintentional interfacial layers that introduce interface traps. The second possible explanation is a mixture layer. It is not clear which mechanism makes a mixture layer, however, the mixture layer is conspicuously formed after laser annealing process as shown in Fig. 5. This observation is consistent with the reports that Ti forms a mixture layer with MoS_2 by placing Ti atoms between the neighboring S planes of MoS_2 and that thermal annealing at 300 °C induces solid-state diffusion in Ti thin film.

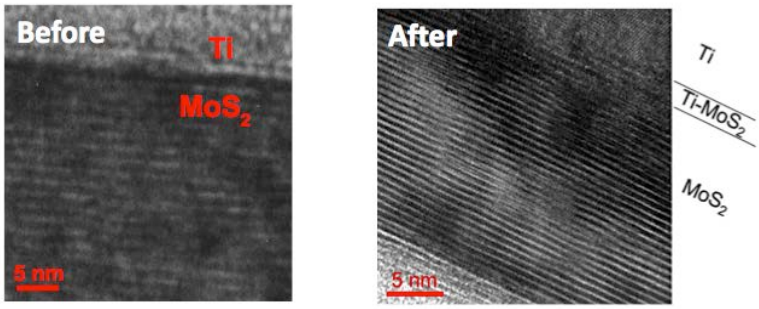

Figure 5: Effect of laser annealing on metal-MoS_2 junction before and after laser annealing. Cross-sectional TEM image showing the mixture layer at the interface after laser annealing.

iii. Electrical characteristics

Fig. 6(a) shows the log- and linear-scale drain current vs. gate-source voltage (I_{ds}-V_{gs}) characteristics for the same MoS_2 TFTs, measured before (black circles) and after laser annealing (red circles) with a power of 18.3 mW). Following selective laser annealing on contacts in MoS_2 TFTs, transistor performance metrics, including on/off-current ratio (I_{on}/I_{off}), peak field-effect mobility ($\mu_{fe} = Lg_m/(WC_{ox}V_{ds})$), subthreshold swing (SS), output resistance (R_o), and voltage-gain for transistor (A_v), were improved. The I_{on}/I_{off} after laser annealing was observed as > 10^6 without a change in I_{off}. μ_{fe} extracted from Fig. 6(a) increased almost two-fold after laser annealing (from 24.84 $cm^2\ V^{-1}s^{-1}$ to 44.84 $cm^2\ V^{-1}s^{-1}$). Here, L, g_m, W, C_{ox} are channel length (L = 7 μm), transconductance, channel width (W = 7.75 μm), and oxide capacitance, respectively. The value of μ_{fe} observed in our MoS_2 TFTs exceeds those reported in previous MoS_2 TFTs on flexible substrates (4.7-24 $cm^2\ V^{-1}s^{-1}$) as well as in organic TFTs or a-Si TFTs on flexible plastic substrates (< 1 $cm^2\ V^{-1}s^{-1}$). Statistically, μ_{fe} of the tested MoS_2 TFTs increased from ~15±10 $cm^2\ V^{-1}s^{-1}$ to ~35±10 $cm^2\ V^{-1}s^{-1}$ after laser annealing. No dependence on channel thickness was observed within the given experimental conditions. Fig. 6(b) shows the drain current as a function of the drain voltage (I_{ds}-V_{ds}) with magnification for the low V_{ds} range (from 0 V to 0.4 V) before (open circles) and after laser annealing (solid circles). At the same V_{gs}-V_{th}, the laser annealing results in ohmic behavior in linear regime and higher current saturation. Following laser annealing, R_o significantly increased to 0.42 MΩ at V_{gs}-V_{th}= 20 V, which is three times higher than values for as-fabricated devices. The most prominent effect of laser annealing is the self-gain ($A_v = g_mR_o$) in MoS_2 TFTs, which exhibits six-fold increase due to enhancement of g_m and R_o. Furthermore, as shown in the Fig. 6(c), we can observe the non linear output curve due to the Schottky barrier before laser process. However, after laser annealing, the curve exhibited linear characteristics. It could be possible to reduce the barrier effect. For supporting the results, we already examined the effects of the laser annealing through the cross-sectional TEM image; the reduction of tunneling barrier width by the formation of a Ti-MoS_2 mixture layer at the interface is thought to be the dominant mechanism of the decreased contact resistance after laser annealing as Ti-doped MoS_2 becomes more conductive due to increased n-type doping. Fig. 6(d) shows the schematic energy band diagram for the MoS_2 transistor at the thermal equilibrium and after laser annealing process. If we assume the existence of a Schottky barrier between metal contacts and a semiconductor, thermionic emission and/or tunneling will allow electron transport during transistor operation. According to Das *et al.*, thermionic emission and tunneling though Schottky barrier limit the

charge injection during off- and on-state of MoS_2 transistors, respectively. The dominant mechanism that reduced contact resistance is not clear as the gate was floated during the measurement of source-drain current. However, the significant increase of the on-current after laser annealing in Fig. 6(a) suggests that laser annealing increases the tunneling current across the Schottky barrier. Since the tunneling current will exponentially increase with $N_D^{0.5}$, where N_D is carrier concentration, the decreased contact resistance after laser annealing is probably due to the reduced tunneling barrier width, which could be resulted from the increased carrier concentration at the interface. To confirm the results and further investigation, we will examine the effect of the laser annealing using YFM in the next section.

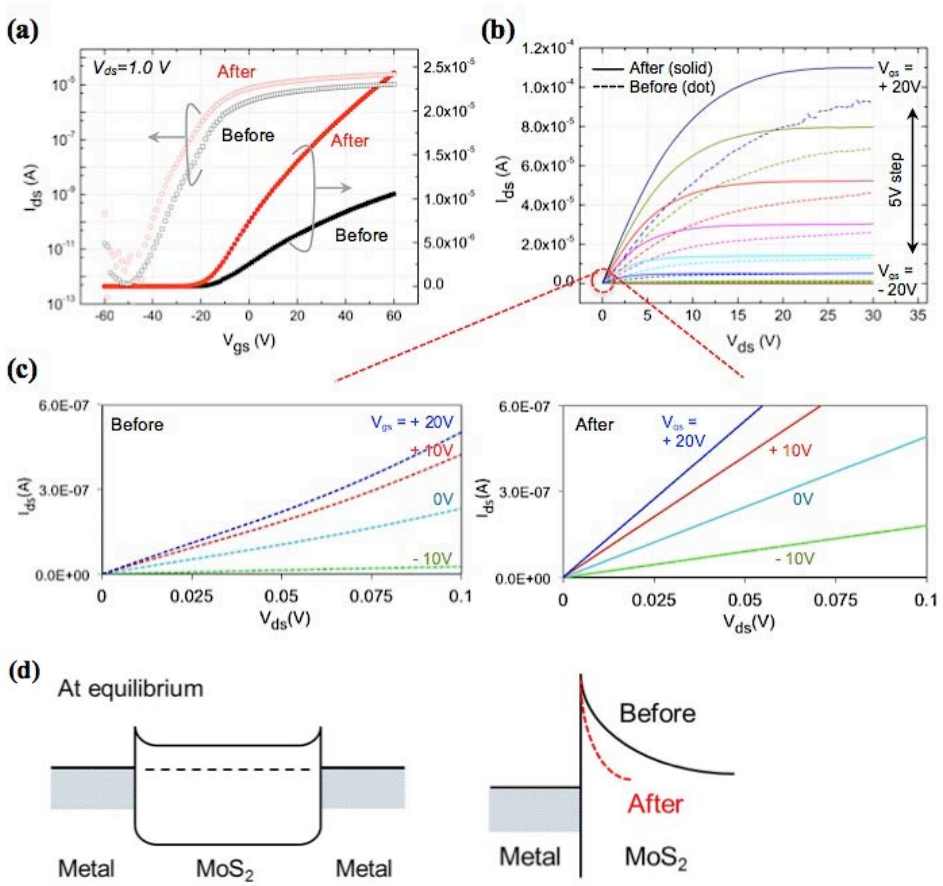

Figure 6: Device performance of MoS_2 TFTs on flexible PEN substrates. (a) Transfer characteristics (I_{ds}-V_{gs}) for the flexible MoS_2 transistor in log-scale (left) and linear-scale (right) before and after laser annealing at V_{ds} = 1 V. (b) Output characteristics (I_{ds}-V_{ds}) before (dot) and after (solid) laser process. (c) Magnifications (before and after) for the low V_{ds} range from 0 to 0.1 V. (d) schematic energy-band diagrams of a multilayer MoS_2 transistors with a Schottky barrier at equilibrium and after laser annealing process.

iv. Y-function method: intrinsic mobility

The field-effect mobility in the linear regime (μ_{eff_lin}) and the μ_0, which characterizes the maximum available mobility without a contact factor in the transistors, were estimated in order to understand the laser annealing impact on the contact conditions or MoS_2 channel layers of the fabricated devices. Normally, to extract the contact resistance of devices, the transfer-line method (TLM) is employed. However, TLM requires several sets of transistors with various channel lengths and uniform contacts.

Furthermore, TLM is quite demanding and difficult to apply in the case of the devices with arbitrary or uncontrollable shapes and very small size channels. Due to this limitation, YFM has been proposed for the extraction of the low-field mobility without the influence of R_c (i.e. the intrinsic mobility, μ_0) and of other parameters (e.g. R_c, mobility attenuator factor (θ), V_{th}) as well. For the YFM, there is no need to make deliberated and calculated devices; the YFM can prove to be a simple and powerful method. The YFM is based on the I_{ds}-V_{gs} relation in the linear region, as below:

$$I_{ds} = g_{ds} \times V_{ds} = \frac{W}{L} Q_{ch} \mu_{eff} \times V_{ds} \tag{3}$$

where g_{ds} is the channel conductance, μ_{eff} is the effective mobility, and Q_{ch} is the channel charge per unit area. Then, we consider the θ ($=\theta_0+\theta^*$), including the contribution from the channel interface (θ_0) and the contact resistance ($\theta^*=\mu_0 C_{ox} R_c W/L$). Therefore, the I_{ds} can be written as,

$$I_{ds} = g_{ds} \times V_{ds} = \frac{W}{L} Q_{ch} \mu_{eff} \times V_{ds} \tag{4}$$

Considering the definition of the transconductance $g_m = \partial I_{ds}/\partial V_{gs},\ V_{ds} = const.$ and the μ_{eff} ($= L g_m/(W C_{ox} V_{ds})$), the Y function can be defined as

$$Y = \frac{I_{ds}}{\sqrt{g_m}} = \sqrt{\frac{W}{L} C_{ox} \mu_0 V_{ds}} \times (V_{gs} - V_{th}) \tag{5}$$

in order to eliminate θ. Note that Eq. (5) is independent of R_c, which is assumed to be constant. It can be seen from Eq. (5) that μ_0 could be extracted from the slope of the Y function, as shown in Fig. 7(a). Using slopes obtained before (5.9×10^{-4}) and after (6.6×10^{-4}) laser annealing, the values of μ_0 are extracted. Fig. 7(b) shows the comparison of the μ_0 and the peak μ_{eff} at the same V_{ds}, +1.0 V. Before the laser process, a large discrepancy (48.18%) exists between μ_0 (37.80 $cm^2\ V^{-1}s^{-1}$) and μ_{eff_lin} (19.59 $cm^2\ V^{-1}s^{-1}$). However, after laser annealing, the discrepancy (2.95%) is greatly reduced: μ_0 (47.31 $cm^2\ V^{-1}s^{-1}$) and μ_{eff_lin} (45.91 $cm^2\ V^{-1}s^{-1}$). To further investigate the laser effects, we extracted the values of θ, and estimated R_c by the following equations:

$$g_m = \left.\frac{\partial I_D}{\partial V_G}\right|_{V_D=const} = \frac{W}{L} C_{ox} \frac{\mu_0}{[1 + \theta(V_G - V_T)]^2} \times V_D \tag{6}$$

For obtaining θ, Eq. (6) can be rewritten as,

$$\frac{1}{\sqrt{g_m}} = \sqrt{\frac{1}{G_m V_D}} \{\theta(V_G - V_T) + 1\} \tag{7}$$

where $G_m = (W/L)\mu_0 C_{ox}$ is the transconductance with the μ_0. From Eq. (7), the values of θ for as-fabricated (1.0×10^{-2}) and after laser annealing (6.3×10^{-3}) can be obtained by the linear fitted slopes (before: ~ 17 and after: ~ 9.6) of the $1/g_m^{0.5}$-V_G curve, as shown in Fig. 7(c). Through the known values of θ, the upper bound of R_c (R_{c_max}) can be calculated when we assume that the influence of θ_0 is negligible. Therefore, the contact effect mainly contributes to θ, and extracted values of R_{c_max} are 28.9 kΩ and

14.6 kΩ, respectively, before and after the laser process. Furthermore, μ_0 is slightly increased (20.10%) before and after the laser treatment. Since μ_0 is not affected by the contact factor, one of the possible reasons for this could be that the quality of the interface is enhanced. The traps between semiconductors and insulators play a critical role in determining the device performance, and the reduced interface trap concentrations were confirmed by the deceased SS values. To reconfirm the results, we roughly estimated the values of channel resistance (R_{ch}) by using the relation $R_{ch}=L/(\mu_0 WC_{ox}(V_G-V_{TH}))$ before and after laser annealing. The obtained values of R_{ch} were 85.34 kΩ (before) and 61.18 kΩ (after), respectively. The results of decreasing R_{ch} by the laser process supports and agrees well with the enhanced interface conditions we described above. Also, through the comparison with R_{c_max} and R_{ch}, we have evidence that the diminishing discrepancy between the μ_{eff_lin} and μ_0 originates from the reduced contact and channel resistance by the laser annealing process. This indicates that the laser annealing process employed is the critical factor involved in enhancing the TFT performance by improving the contact conditions and promoting the interface quality without thermal damage to plastic substrates.

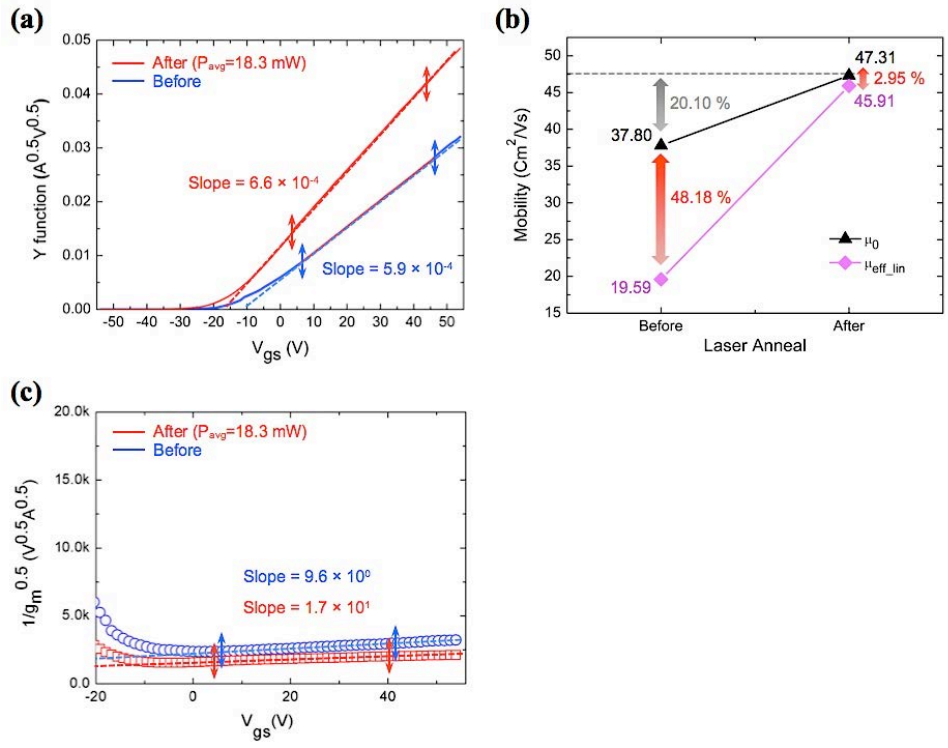

Figure 7: Y function and evaluation of electrical parameters before and after the laser process. (a) Plots of Y function with respect to V_{gs} and the linear fitting in the strong accumulation region for obtaining the slope. (b) Comparison of the low-field mobility (μ_0) and peak field effect mobility (μ_{eff_lin}) before and after the laser process. (c) Plots of $1/g_m^{0.5}$ with respect to the V_{gs} and their slopes in the straight line fitting for extraction of the mobility attenuation factor (θ).

v. Variability of electrical contact properties

In Korea collaborators, to obtain more information on the metal-MoS_2 junction, they measure the I-V characteristics of the two MoS_2 transistors at increased temperatures up to 240 °C. Fig. 8(a) shows the transfer characteristics of the two MoS_2 transistors at five different temperatures (room temperature, 60 °C, 120 °C, 180 °C and 240 °C). Since the two transistors have different channel widths and thicknesses, drain current

density (J_d) is used for comparison instead of I_d. (Sample A: L = 10 μm, W = 10 μm, and thickness of MoS_2 channel t = 31 nm, Sample B: L = 10 μm, W = 35 μm, t = 63 nm).

For both transistors, off-current density (J_{off}) and subthreshold swing significantly increase with increased temperature as J_{off} is known to be dominated by thermionic emission and subthreshold swing is proportional to kT (k: Boltzmann constant, T: temperature). While J_{off} of the two transistors are comparable at each temperature, the on-current density (J_{on}) of Sample A is higher than that of Sample B by an order of magnitude. This suggests significant difference in tunneling barrier width between the two transistors as tunneling is known to dominate the on-current of MoS_2 transistors. To support this argument, they estimate the Schottky barrier height (Φ_B) of Samples A and B at flat band condition. They build a series of Arrhenius plot in Figs. 8(b) and 8(c) with the data in Fig. 8(a). Then, assuming the conventional thermionic emission theory, they obtain effective Schottky barrier height at a specific V_g in Fig. 8(d) from the slope of the data in Figs 8(b) and 8(c). In thermionic emission theory, J_d is related to Φ_B through the expression $J_d = A^* T^2 \exp(-q\Phi_B/kT) [\exp(qV_d/kT) - 1]$, where A^* is Richardson constant, q is the elementary charge, and T is temperature. The Φ_B at flat band condition can now be readily estimated in Fig. 8(d). The obtained Φ_B of Samples A and B at flat band condition are relatively close (41 meV and 50 meV, respectively). The estimated Φ_B in this study is comparable with the reported Φ_B of Ti-MoS_2 in literature (50-65 meV).

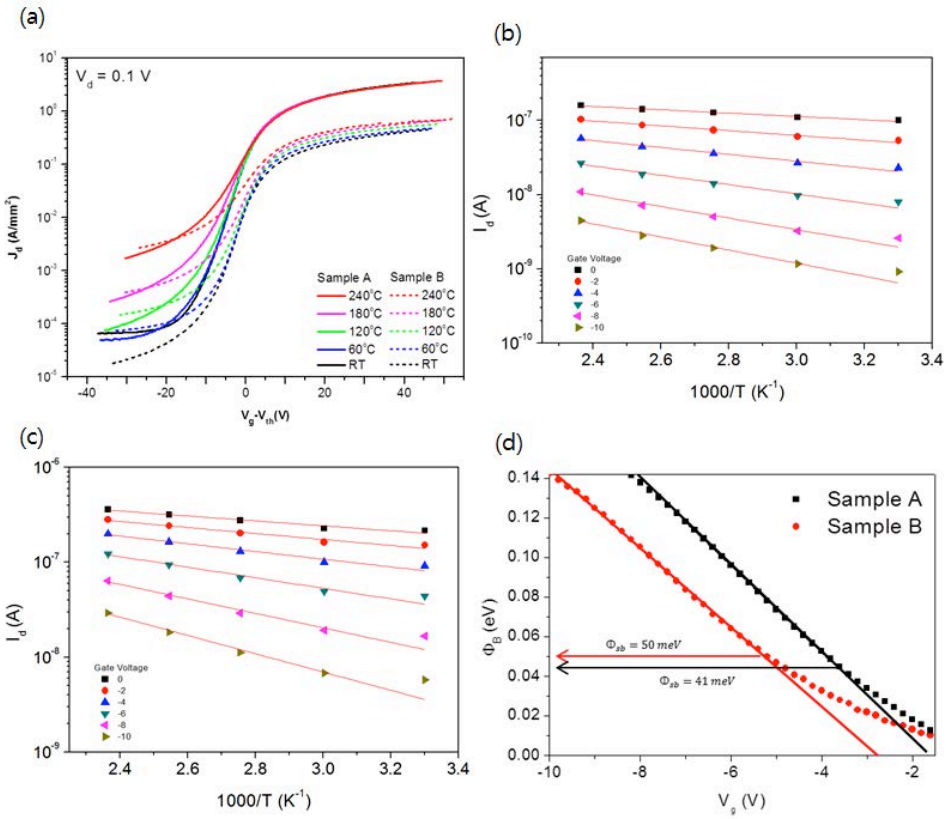

Figure 8: (a) Transfer characteristics of two MoS_2 transistors (Samples A and B) at different temperatures. Drain current density (J_d) is used for comparison due to the differences in channel width and length of the two transistors. (b) Arrhenius-type plot of Sample A created by the data in (a). (c) Arrhenius-type plot of Sample B created by the data in (a). (d) Extracted effective barrier height of Samples A and B as a function of applied gate voltage.

Fig. 9 shows the extracted field effect mobility of Samples A and B from room temperature to 240°C. At this temperature range, theoretical calculation indicates that optical phonon scattering dominates the transport of multilayer MoS_2 crystals with ohmic contacts. The mobility of Sample A slightly decreases from 31 $cm^2V^{-1}s^{-1}$ to 29 $cm^2V^{-1}s^{-1}$ with increasing temperature exhibiting a typical signature of band transport. However, the mobility of Sample B increases exponentially (from 5 $cm^2V^{-1}s^{-1}$ to 11 $cm^2V^{-1}s^{-1}$) for the same temperature range suggesting a thermally activated transport. Three possible sources can explain the observed thermally activated behavior of Sample B in Fig. 9: the existence of grain boundaries in the MoS_2 channel, the existence of Schottky barriers at the Ti-MoS_2 junction, or the existence of high concentration of trap states in the MoS_2 channel. With the existence of grain boundaries ruled out due to the single crystal MoS_2 channel, the more likely source is the existence of Schottky barriers. Then, the distinct transport behavior in Fig. 9 can be understood by the energy band diagram shown in the inset of Fig. 9.

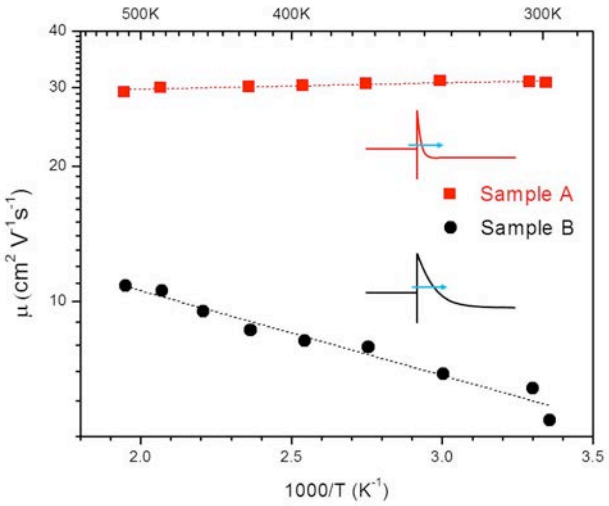

Figure 9: Field effect mobility of Samples A and B as a function of inverse temperature. Inset shows schematic energy band diagrams of Samples A and B at the Ti-MoS_2 junction.

When the conduction band moves upward at negative gate voltages, the increased barrier height prevents electron transport from metal to MoS_2. Since this off-current is dominated by thermionic emission and both samples have similar barrier height, the off-current in Fig. 9(a) is similar for each sample. When the conduction band moves down at positive gate voltages, the barrier height remains the same for each sample due to Fermi level pinning. Yet, as the on-current is dominated by thermally-assisted tunneling, Sample A will have a much narrower barrier width than that of Sample B allowing an enhanced tunneling current across the barrier. Therefore, the mobility of Sample A shows the dominant contribution of MoS_2 channel resistance with negligible effect of the Ti-MoS_2 junction. The existence of highly-doped region such as metallic TiS_2 or Ti-doped MoS_2 has been observed at the Ti-MoS_2 junction. However, due to the wide Schottky barrier, the mobility of Sample B is dominated by the contact resistance at the Ti-MoS_2 junction.

Since the tunneling current will exponentially increase with $N_D^{0.5}$, where N_D is carrier concentration, significant difference in carrier concentration will exist at the Ti-MoS_2 junction between Sample A and Sample B. Such a variable carrier concentration at the Ti-MoS_2 junction could be related to the non-uniform distribution

of metallic defects, assumed to be clusters of S vacancies, in naturally-occurring MoS_2 crystals. The variation of defect density in MoS_2 could induce the variation of carrier concentration in MoS_2, which can cause the variation of Schottky barrier width at the Ti-MoS_2 junction. Hence, the variation of defect distribution in MoS_2 crystals may eventually lead to the different behavior of mobility depicted in Fig. 9.

b. Laser doping

i. Laser doping of monolayer MoS_2 and WSe_2: tuning the optical properties

The PL spectrum of monolayer MoS_2 and WSe_2 before and after the laser phosphorus doping is shown in Fig. 10(a). The peak PL intensity of the laser-doped area is approximately order of magnitude greater and lesser than that of the as-prepared monolayer MoS_2 and WSe_2, respectively. The spectral distribution of the PL peak also sharpens upon the laser phosphorus doping while the peak energy of the PL spectra in monolayer MoS_2 was blue-shifted by approximately 32 meV, as explained by the contributions of the exciton (X, e-h pair) and the negative trion (X-, e-e-h clusters) in the PL peak. The PL peak location is consistent with the positions of the exciton peak (X; ~1.88 eV, e-h pair) and the negative trion peak (X-; ~1.84 eV, e-e-h pair). For the as-prepared monolayer, the PL contribution of the negative peak (X-) that is positioned at 1.84 eV is higher than that of the exciton peak (X), positioning. However, in the PL spectra of monolayer MoS_2 after phosphorus doping by laser, the exciton peak (X) contribution dominates the effect of the negative trion peak (X-) due to recombination of excess carriers (electrons in MoS_2) by hole injection from the incorporated phosphorus. The blue shift of the PL spectrum is thus consistent with p-doping effect. The p-doping effect on intrinsically n-type MoS_2 displays largely different effects (Fig. 10(b)) compared to intrinsically p-type materials, WSe_2 (Fig. 10(c)). The as-exfoliated monolayer WSe_2 exhibits direct band gaps at 1.67 eV. Upon phosphorus doping, the PL intensity of WSe_2 is drastically reduced since incorporated excess hole carriers strongly suppress the exciton emission. The spectral shape of peak becomes broader after the laser phosphorus doping. The PL spectra peaks in monolayer WSe_2 was red-shifted approximately 45 meV, as can be explained by considering the contributions of the exciton (X, e-h pair) and the positive trion (X+, e-h-h clusters).

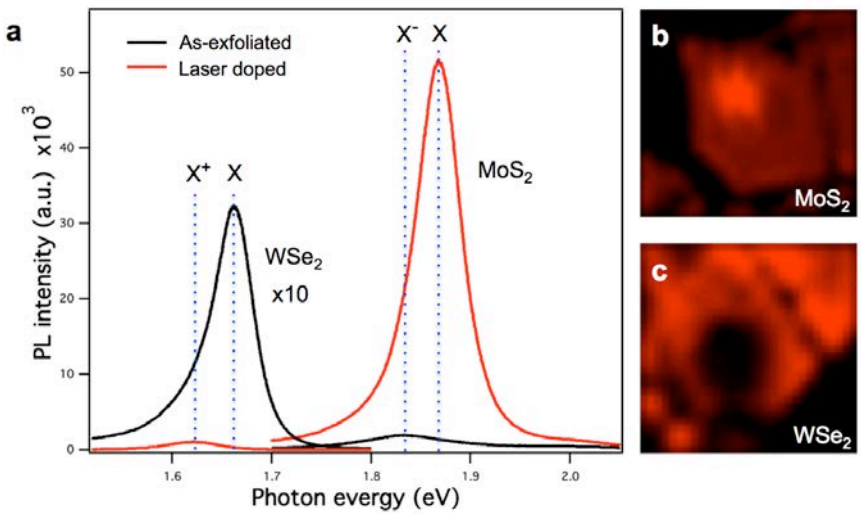

Figure 10: Photoluminescence (PL) spectra of monolayer WSe_2 and MoS_2 before and after laser assisted doping with phosphorus as a p-type dopant (a) and its PL mapping images of WSe_2 (b) and MoS_2 (c).

The Gaussian profile of the laser beam intensity is expected to generate a spatially varying temperature distribution at the irradiation spot. Although various reports have been published on optical and thermal properties of TMDC materials, there is still insufficient information to enable accurate prediction of the induced temperature in our laser doping process. The maximum PL intensities across the laser doped regions in the monolayers MoS_2 (Fig. 11(a) inset) and WSe_2 (Fig. 11(b) inset) are plotted in Figs. 11(a) and 11(b). These distributions could be fitted to a Gaussian profile, suggesting that the hole doping concentration increases with doping temperature, which maximizes at the center of the laser reaction spot. The full width half maximum (FWHM) of the PL intensity profile was approximately 2.5 µm, which is in agreement with the focal spot size of ~2.3 µm, considering the 10× and 0.28 NA lens and the 532 nm laser light wavelength. Fig. 11(c) inset shows that for MoS_2, the PL gradually shifts weight from X^- to X emission as the reaction spot is scanned from the edge to the center. In contrast, the WSe_2 shows a transition from X to X^+ (Fig. 11(d) inset).

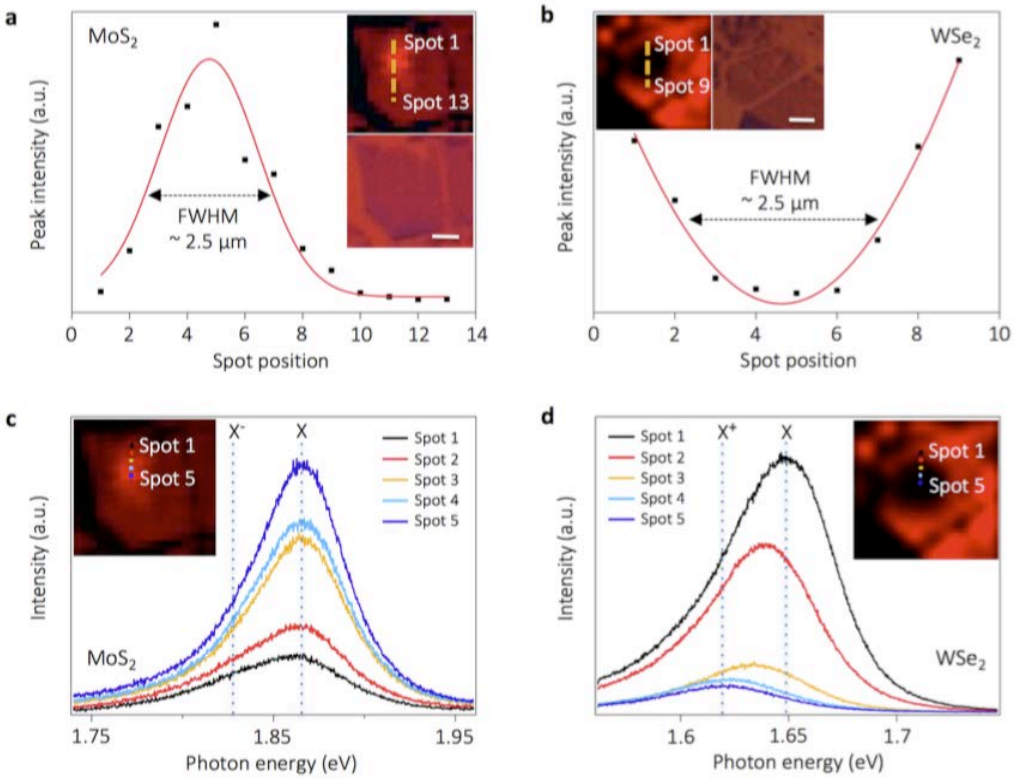

Figure 11: PL peak intensity line profile of laser assisted doping monolayer (a) MoS_2 and (b) WSe_2 at the reaction spot. Inset images show the PL peak intensity-mapping image and optical microscopy image of the laser-doped region. Scale bars are 2 and 5 µm, respectively. Variation of the PL intensity within the single spot of laser doped monolayer (c) MoS_2 and (d) WSe_2. Inset shows the PL mapping image. The spacing between each spot is 500 nm.

ii. Nano-Auger electron spectroscopy

To study the mechanisms of the laser-assisted doping process, nano-Auger electron spectroscopy (nano-AES) which enables local chemical analysis using focused electron beam of ~10 nm spot size at ultra-high vacuum of base pressure ~10^{-10} mbar (Oxford/Omicron system) was performed on pristine and laser-doped regions of MoS_2 crystals at various doping conditions such as irradiation time, doping gas composition,

and laser power. Considering that AES reflects in the chemical properties of the material surface within a depth of few atomic layers, multilayer and tri-layer MoS_2 flakes were chosen as model strictures analogous to monolayers to explore the role of laser heating during doping process. In Fig. 12(a), the S/Mo Auger signal ratio of the multilayer MoS_2 layer is slightly reduced by 10 sec and 30 sec irradiation implying that chalcogen vacancies are created at low density, while it can be clearly shown that the S/Mo ratio decreases significantly and the Auger transitions of P atoms are shown up after 60 sec irradiation. The drastic changes in Auger spectra occurred between 30 sec and 60 sec. Therefore, it is presumable that the phosphorous atoms were directly deposited on the MoS_2 surface after 30 sec laser irradiation via the dissociation of PH_3 dopant molecules accelerated by the heat accumulation. Surface roughness change after irradiation for 60 sec was also confirmed by AFM scanning. Also, Fig. 12(b) clearly shows that as the concentration of PH_3 dopant gas balanced with Ar is higher (i.e., Ar flow rate is set lower), the S/Mo ratio of the multilayer MoS_2 flake is decreased more after laser irradiation.

Further, the laser-assisted doping reaction in the 2D regime has been analyzed quantitatively by performing nano-AES on MoS_2 tri-layers as summarized in Fig. 12(c). The P doping level, *[P]/([P]+[S])*, was estimated to be 4.68 at.% and 56.04 at.% from the tri-layers that were laser- doped at 180 mW and 200 mW respectively while the doping duration time was set as 60 sec for the both cases. In the case of 200 mW process, P atoms seem to be deposited on the MoS_2 surface excessively, which gives a very similar result with the cases when the laser power or gas composition are set higher than threshold values as described in Figs. 12(a) and 12(b).

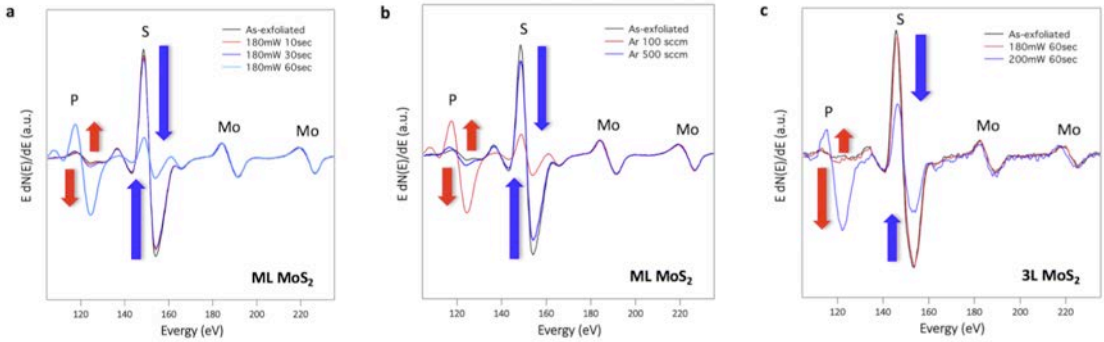

Figure 12: (a) Auger electron spectroscopy spectra taken before and after the doping at a range of laser irradiation times (10, 30, and 60 sec at 180 mW with multilayer MoS_2), (b) dopant concentration by argon dilution (flow rate of 100 and 500 sccm with multilayer MoS_2), and (c) laser irradiation power (180 and 200 mW at 60 sec with tri-layer MoS_2).

iii. Laser doping of bilayer MoS_2 and WSe_2: tuning the electrical properties

In parallel to strong modification of the luminescent properties, the laser-assisted doping also imposes drastic effects on electrical properties of the ultra-thin TMDCs. This was investigated using field effect transistor (FET) devices incorporating the locally-doped TMDCs layers as current channels. As displayed in Figs. 13(a) and 13(c), multiple electrodes was patterned onto TMDC bilayer flakes, covering both pristine and laser-doped regions. A voltage applied through the back gate provides additional modulation of carrier density in the TMDC channel. In the undoped regions, n-type (p-type) FET behavior was observed with on-off ratio exceeding five orders of magnitude from the MoS_2 (WSe_2) bilayers. The FET characteristics, *i.e.*, source-drain current (I_{SD}) versus back gate voltage (V_G) curves, of devices fabricated with different

distance from the center of the laser-doped region, change gradually in a manner consistent with the spatially-graded variation of PL across the same region, as summarized in Figs. 13(b) and 13(d). The phosphorous doping suppresses the n-type characteristics of the MoS_2, and enhances the p-type characteristics of the WSe_2 drastically, with increase in conductance as well as shift of threshold voltage. The hysteresis features of FET loops are likely due to water molecule absorption on the surface of the TMDCs, considering that all electrical measurements were conducted under ambient conditions.

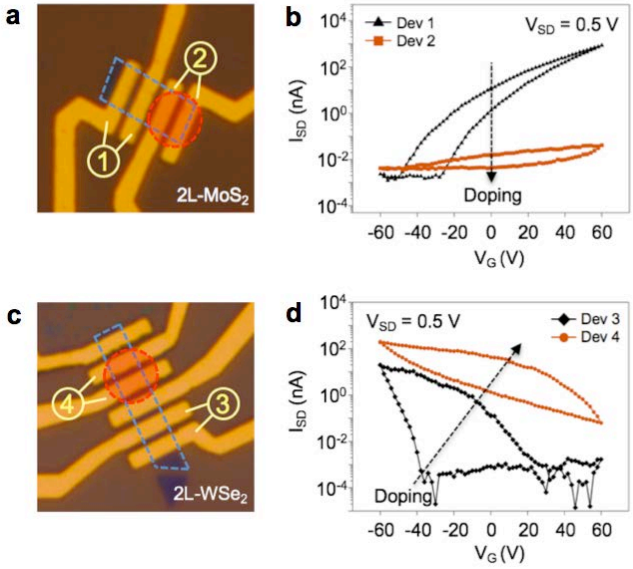

Figure 13: Bilayer MoS_2 and WSe_2 FET device (a), (c) the flakes are outlined by the blue dashed box and the laser irradiated area is denoted by the red dashed circle. Source-drain current (I_{SD}) versus back gate voltage (V_G) curve recorded from the device in (a) and (c) with a bias voltage of 500mV (b), (d)

iv. Long-term stability of the laser-assisted phosphorus doped MoS_2

Reliable performance of devices requires stable doping of the active materials. Indeed, previous studies have already achieved both n- and p-type doping by surface charge transfer mechanisms, mostly through chemical physisorption. However, physisorption doping is unstable and decays almost completely within an hour, or is retained for longer periods only if the doping environment is maintained or protected. Among the various doping methods, substitutional doping of foreign elements is an effective and stable doping strategy for TMDCs. In our work, the laser was used to create sulphur vacancies and locally heat up the material to crack the precursor molecules, enabling the substitution of sulphur with phosphorous. The PL data in Fig. 14(a) shows that the laser-assisted doping is irreversible and stable, even after exposure in air for a month. As a comparison to test the doping stability, we also studied a laser annealing effect. In this case, the monolayer MoS_2 was laser irradiated in absence of the dopant gas at the given laser conditions (i.e. the exact same conditions used for doping). As shown in Fig. 14(b), the PL intensity of monolayer MoS_2 increases right after the laser annealing, as in the case of laser doping. However, the PL intensity increase was higher than the increase in the case of laser doping. After one week, however, the PL intensity drastically drops and continues to drop to the original value within 2 weeks, indicating instability of the laser annealing effect, and the necessity of the presence of the PH_3 molecules for stable doping.

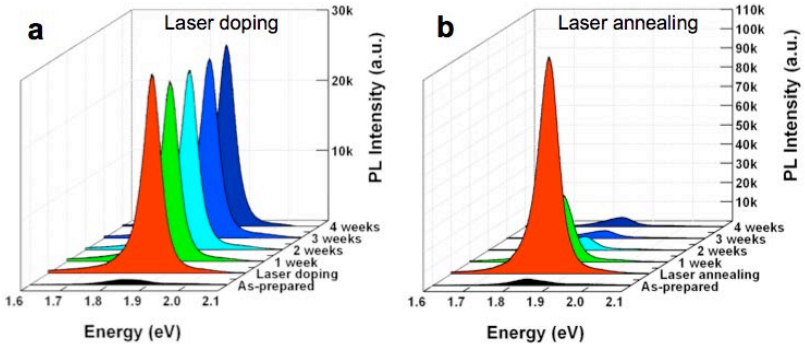

Figure 14: (a) PL spectra of laser assisted phosphorus-doped monolayer MoS_2 and (b) laser annealed with the same condition of doped one. The samples are under exposure to oxygen and water molecules in ambient air.

c. Laser welding

i. Plasmonic laser welding

The electrical contact at the Ag NW junctions can be improved by laser welding, which is based on highly localized heating induced by plasmonic effects. Fig. 15(a) illustrates the schematic concept of the laser welding process for the 2D-like random networks of Ag NWs. In this research, as-prepared 2D-like Ag NW networks showed unfavorable electrical sheet resistance, 480 ~ 550 Ω/□, due to weak physical contact between nanowires (in the left-bottom inset of Fig. 15(a)). Here, we note that even though different sheet resistance can be produced by tuning the nanowire diameter, length, and surface coverage of nanowires, we applied laser process under ambient condition to enhance the electrical properties of the interconnected wires (in the right-bottom inset of Fig. 15(a)), without requiring precise control of the dimensions or the number density of the Ag NWs.

After the laser welding process, the sheet resistance was drastically reduced by 10 ~ 15 Ω/□; these values were almost 37 or 55- fold lower than for the as-prepared samples. To confirm this finding, we took SEM images before and after laser irradiation as shown in Figs. 15(b) and 15(c). The results clearly indicate that the laser process induced fusion (red circles) at the NW junctions (Fig. 15(c)) in contrast to the as-prepared NW junctions (Fig. 15(b)). The features of laser welding process for creating the interconnected mesh are well described by considering the plasmonic effect at Ag NW junctions that form a naturally small gap. The concentrated photon source induces localized heat spreads into the NWs due to their high thermal conductivity. The small gaps at the NW junctions enable selective and effective focusing of light and heating (to sufficiently high temperature to soften/melt the outer NW surfaces), right at the contact. We could find evidence of the locally generated plasmonic effect generated in the small gap configuration from the morphological changes of the NWs. As shown in the inset of Fig. 15(c), after the laser illumination, the morphology of only the NW junction substantially changed; NWs slightly melted and joined via welding. On the other hand, the morphology of NWs away from the junction did not change unlike in the junction proximity. If the thermal distribution were uniform on the NWs, morphological changes would be observed over their entire lengths. Therefore, this laser welding process was different from conventional, uniformly distributed thermal heating. The locally generated plasmonic effect can also prevent damage to low thermal budget plastic substrates.

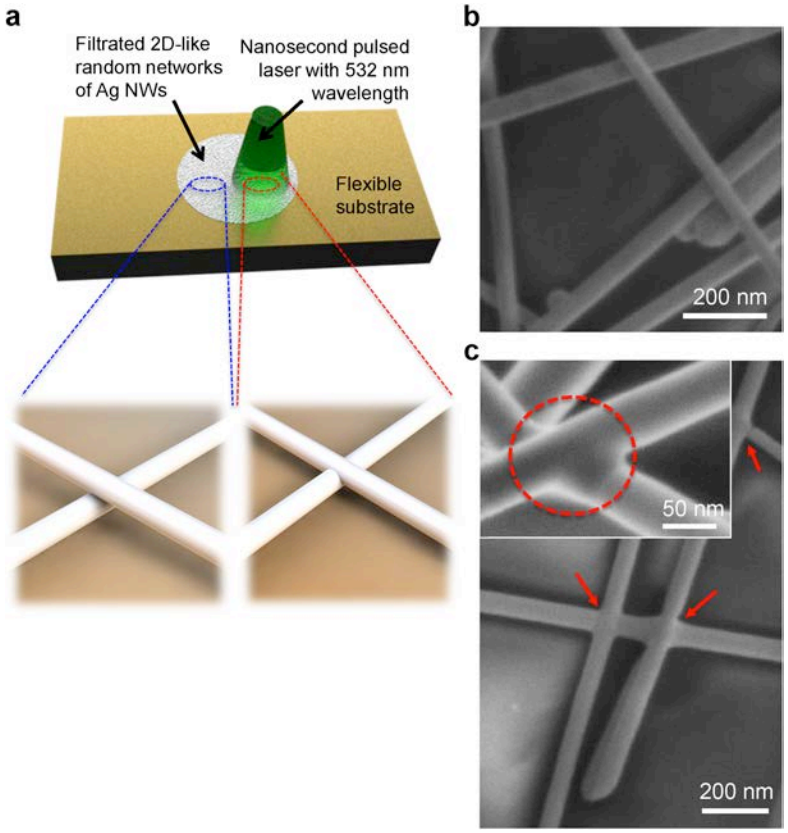

Figure 15: Plasmonic nanowelded metal NWs network for flexible gate electrode. (a) The schematic concept of the laser welding process for Ag NW network on the PI substrate formed by filtration method. The bottom insets show schematic illustrations of the junctions between two adjacent NWs [Left] before and [Right] after laser treatment. (b-c) SEM images of (a) as-prepared Ag NWs random networks before laser welding and (c) after the laser treatment (red arrows indicate the laser welded junctions). The inset shows the magnified SEM image of laser-welded part.

ii. Solution based embedded PI structure

Laser welding treatment makes conductivities of the Ag NW films less susceptible to external mechanical stress, but considerable surface roughness still persists. A possible solution to this issue is to embed the Ag NW electrode into the substrate, which also eliminates the film–substrate adhesion problem.

For a flexible substrate, solution-type PI is spin-coated onto the laser-treated Ag NWs network, resulting in the permeation of PI into the voids formed between the Ag NWs owing to its low viscosity and surface energy. As a result, the Ag NWs are partially embedded and held firmly within the flexible PI substrate with their initial positions and corresponding contacts remaining intact under varying mechanical stress.

Fig. 16(a) compares the atomic force microscope (AFM) images of as-deposited, normal (i.e., not-embedded) Ag NWs on a rigid glass substrate and partially embedded Ag NWs in a PI substrate. Individual NWs are clearly identified in the top AFM image in Fig. 16(a). However, the surface morphology and roughness change dramatically when the Ag NWs are partially embedded in the PI, exhibiting a much smoother surface with reduced roughness as shown in the bottom AFM image. These results are also confirmed in the topological line profile (Fig. 16(b)). Root-mean-squared heights for normal and embedded Ag NWs are found to be ≈39.0 nm and 6.0 nm, respectively.

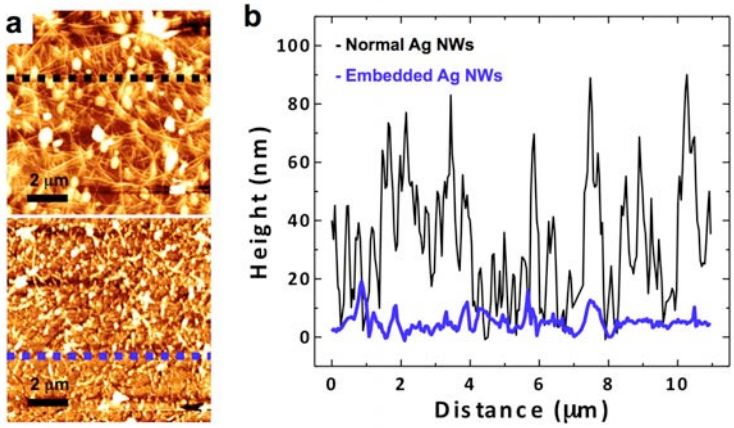

Figure 16: Solution based embedded polyimide (PI) structure. (a) 2D AFM images of the Ag NWs as-deposited either on a rigid glass substrate, i.e., not embedded (top), or partially embedded in the PI substrate (bottom). (b) Topological line profile data obtained along the black/blue dashed lines in (a).

iii. Numerical simulation of nonlinear hyperelastic materials

The mechanical behavior of hyperelastic materials (*e.g.*, PI, PEN, PET, polymer, or rubber-like materials) is generally expressed in terms of strain energy potential. Furthermore, many different models have been suggested to define the strain energy function for predicting the properties of hyperelastic materials. Therefore, in order to come up with a proper model that describes well the mechanical characteristics of the flexible MoS_2 devices with hyperelastic substrate, different hyperelastic models must be compared with the real experimental data. Fig. 17(a) shows the measured stress(σ)–stretch(λ) curve of a specimen with a thickness (t) of 0.105 mm, fabricated with solution based PI and PET. Under static and cyclic bending test, the strain (σ) represents the amount of force per unit area, and the engineering stretch (λ) represents the relative elongation:

$$\lambda = \frac{(L_0 + \Delta L)}{L_0} = 1 + \varepsilon \tag{8}$$

where ε is the engineering normal strain. From the experimental data, an ultimate tensile stress of 46.6×10^6 N m^{-2} is observed at a maximum elongation of 43% (λ = 1.43). Also, within the moderate strain range of interest (< 10%, λ = 1.10), the Mooney-Rivlin model is found to match well with our experimental data as shown in the inset of Fig. 17(a). The two-parameter Mooney-Rivlin model assumes that the local strain energy density in an incompressible material is a simple function of local strain invariants. For uniaxial loading, the nominal stress-stretch behavior for the Mooney-Rivin model, is given by:

$$\sigma = \frac{F}{A_0} = 2\left(C_{10} + \frac{C_{01}}{\lambda}\right)\left(\lambda - \frac{1}{\lambda^2}\right) \tag{9}$$

where A_0 is the cross-section area of the test specimen and L_0 is the original length of the specimen. The two-parameters, C_{10} and C_{01}, are material parameters determined by fitting the model (Eq. (9)) to the experimental data (blue dot in the inset of Fig. 17(a)). Through the model, the stress state in a cross section of the flexible substrate

mounted on a mechanical bending tester can be simulated, as shown in Fig. 17(b).

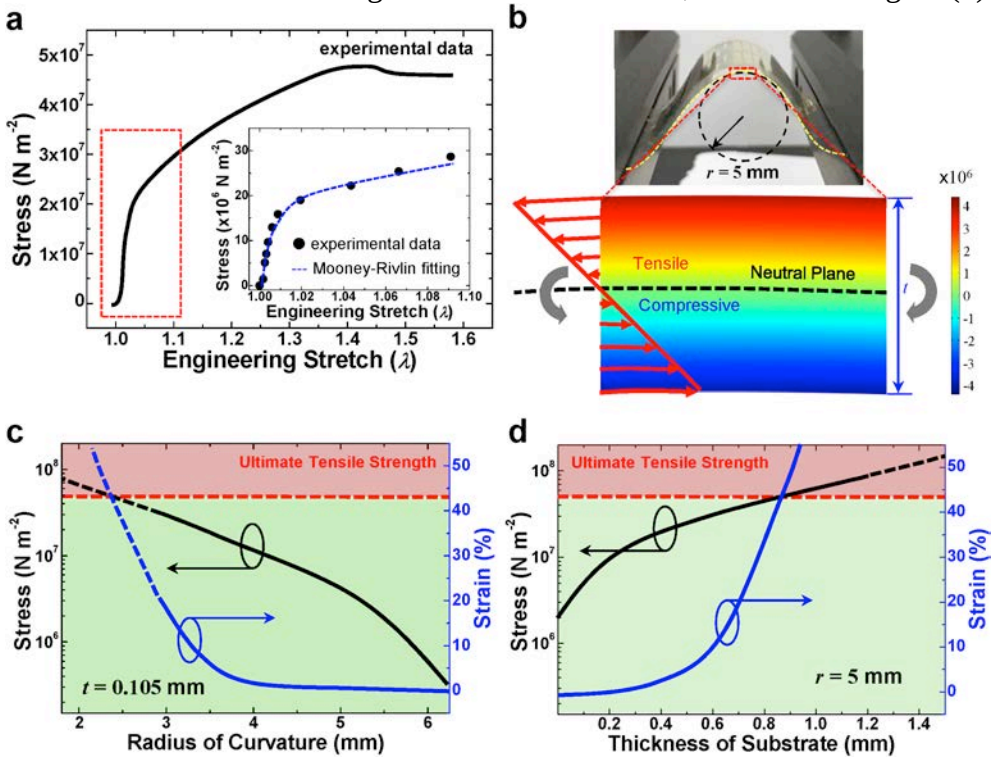

Figure 17: Computational non-linear hyperelastic analyses on the mechanical bending stress of the flexible MoS_2 TFT. (a) Measured stress(σ)–stretch(λ) curve of the specimen of solution based PI and PET (t = 0.105 mm). The inset shows experimental data fitted with Mooney-Rivlin model. (b) The numerical result on hyperelastic nonlinear stress analyses based on the parameters extracted from the experimental data when the bending radius is 5 mm. The top inset shows a photograph of the bent MoS_2 TFTs with a radius of 5 mm. (c-d) Based on the Mooney-Rivlin model, the expected mechanically stable range (green region) of the structure with respect to the (c) radius of curvature of the substrate and (d) thickness of the substrate.

To investigate the flexible structure, hyperelastic nonlinear stress analysis is performed through COMSOL Multiphysics. It is generally known that when an elastomeric slab is bent with arbitrary radius r, there exists a neutral plane (*i.e.*, stress-free zone) in the geometric mid-plane. The computational result shows that the outer surface of the specimen is under tensile stress and the inner surface in under compression, with respect to the neutral plane where the material experiences no stress (Fig. 17(b)). When the bending radius (r) was 5 mm, the maximum internal tensile stress induced in the outermost region (interface between Ag NWs network and PI substrate) is 4.38×10^6 N m^{-2}. This induces a total strain of 0.2% in the substrate. Such small strain induced in the PI upon bending indicates that the devices also undergo relatively small mechanical strain levels, and so the electrical properties are affected to a very small extent. To understand the correlation between the bending radius and the induced stress in detail, calculations were performed with respect to the bending radius and the substrate thickness. Through such a procedure, one may predict a range of device dimensions over which the system is mechanically stable. As show in Fig. 17(c), the flexible structure is anticipated to tolerate a specific range of stress (green region, $r > 2.5$ mm at t = 0.105 mm) without reaching the failure stress (4.66×10^7 N m^{-2}) and elongation (43%). Note that the results based on the Mooney-Rivlin model do not guarantee device stability at relatively large strains

(marked with dotted lines). Also, when the substrate thickness t is larger than 0.8 mm (at r = 5 mm), the structure can be destroyed (Fig. 17(d)). Therefore, in order to remain in the mechanically stable state, the generated stress must be kept below the ultimate tensile strength (red region). Additional parameters, such as the thicknesses and mechanically properties of each individual layer (*e.g.*, dielectric, semiconductor, electrodes, etc.), as well as their structure must also be optimized so that functional devices can be achieved. When ductile materials such as metals having very low elastic region (only 0.2 or 0.3% strain) are used, the structure becomes more vulnerable to the bending so a more meticulous design is mandatory. In this regard, laser welded Ag NWs network can thus be preferential over metal layers, not only for the flexible but also stretchable electronics.

iv. Variation of TFT performances under mechanical stresses

For investigating solid tolerance of our flexible MoS_2 TFTs against various mechanical stresses, two kinds of tensile stresses were applied to the flexible TFTs array parallel to their active channels; static and cyclic upward bending (Insets of Figs. 18(a) and 18(b)). The lamination of a 100-μm-thickness PET film beneath the PI substrate enables the downshift of neutral plane in the flexible MoS_2 TFTs array, so that the entire TFT could lie within the tensile-stress zone. As a result, the flexibility of our devices can be investigated under relatively harsher environments.

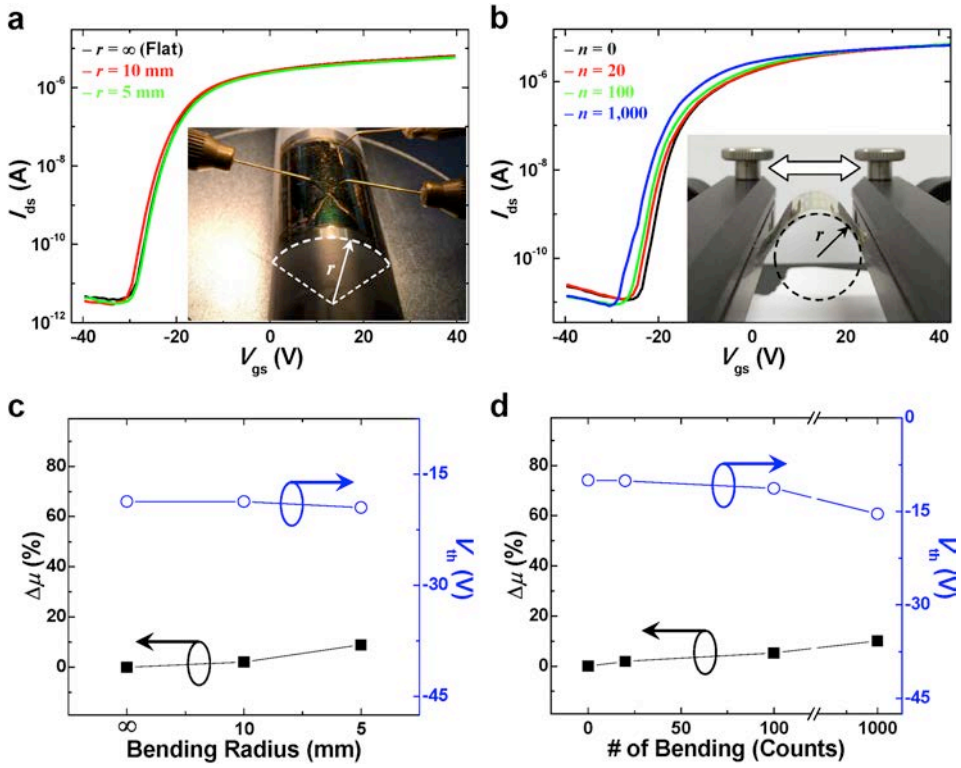

Figure 18: Variation of MoS_2 TFT performances under various mechanical stresses. (a) Comparison of the transfer characteristics of the flexible MoS_2 TFTs under static bending environments with three different bending radii (flat, r = 10 mm, and 5 mm). The inset shows a photograph of the bent MoS_2 TFTs attached on rigid cylinder with a pre-defined radius (white dashed arc and arrow). (b) Comparison of the transfer characteristics under cyclic bending with respect to number of bending (n = 0, 20, 100, and 1,000). The inset shows a photograph of the flexible MoS_2 TFTs loaded on a multi-modal bending tester. The cyclic bending radius was fixed at 10 mm (black dashed circle and arrow). (c-d) Variations of μ_{eff} and V_{th} of the flexible MoS_2 TFTs as a function of the

(c) static bending radii and (d) number of cyclic bending.

Fig. 18(a) compares the transfer characteristic curves of the MoS_2 TFTs array under flat and statically bent conditions. The I_{ds}–V_{gs} curves of the MoS_2 TFT with bending radii of 10 and 5 mm did not change significantly with respect to that in the flat condition. The variation of the mobility values ($\Delta\mu$ (%) = $|\mu_{bending} - \mu_{flat}| / \mu_{flat}$) due to the bending with r = 10 and 5 mm are estimated to be 2.0% and 8.8%, respectively (Fig. 18(c)). The threshold voltage (V_{th}) of the MoS_2 TFT in the flat condition is -18.7 V. For r = 10 mm, the V_{th} just remains identical to its initial value, and shifts to -19.5 V when r = 5 mm. Fig. 18(b) shows a comparison of the transfer characteristics of another MoS_2 TFT under cyclic bending. As the number of bending (n) increases, the entire I_{ds}–V_{gs} curves shift slightly toward negative V_{gs} value. However, the I_{on} / I_{off} ratio is preserved to ~10^5. The $\Delta\mu$ (V_{th}) due to the cyclic bending with n of 20, 100, and 1,000 are 1.9% (-10.1 V), 5.3% (-11.3 V), and 10.0% (-15.4 V), respectively (Fig. 18(d)). It should be noted that the thin ALD Al_2O_3 layer plays an important role in our flexible TFTs array, by enhancing the adhesion between the GI and the S/D electrodes as well as active layer. MoS_2 TFTs without Al_2O_3 layer exhibited poor transistor performance under identical bending conditions.

d. High-mobility transistors based on large-area and highly crystalline CVD-grown 2D films

The uniform growth of large grain multilayer $MoSe_2$ films on insulator substrates was demonstrated using a modified chemical vapor deposition method. Highly crystalline $MoSe_2$ film with large grain sizes was fabricated as an active channel for a transistor, consisting of bottom gate architecture with Ti/Au source and drain, on flexible plastic substrate or a rigid Si wafer.

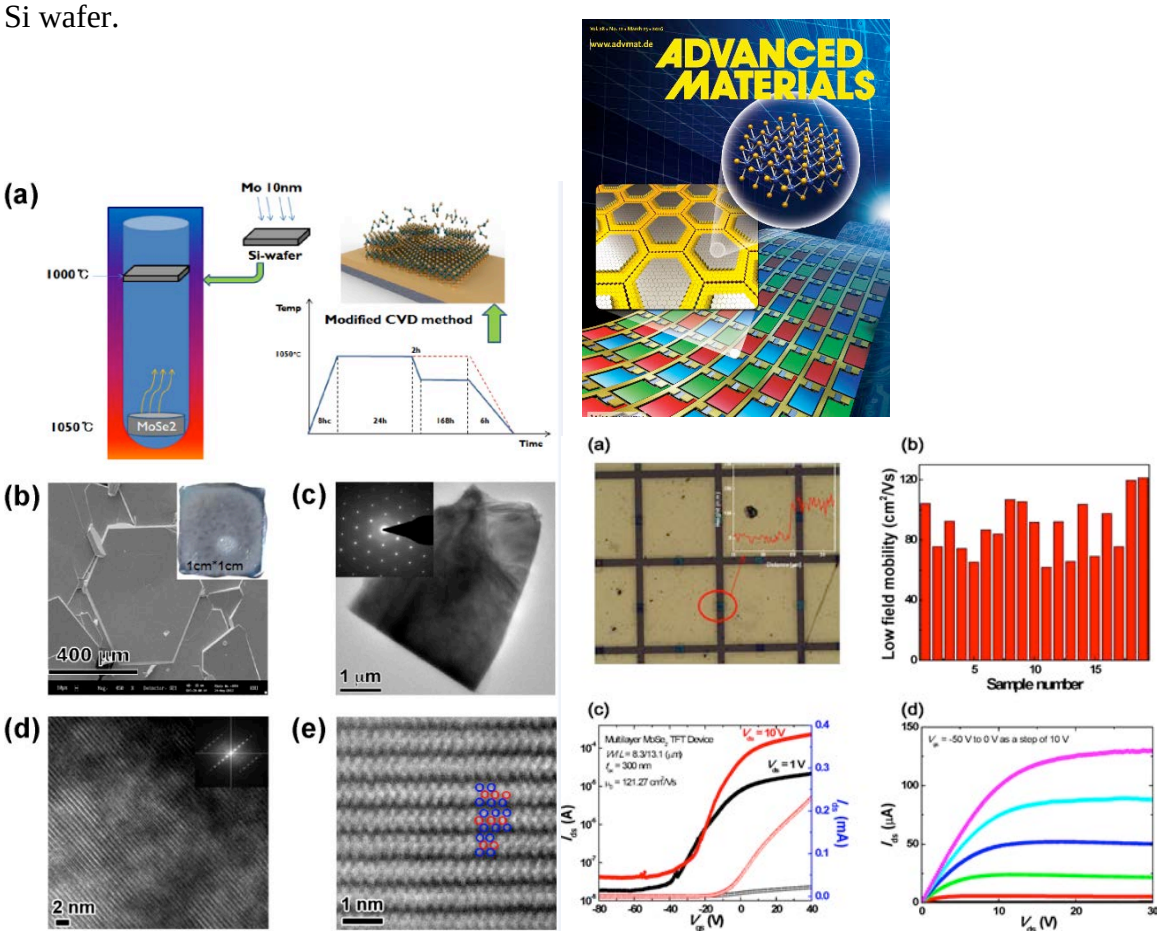

Figure 19: Synthesis and microstructure of $MoSe_2$ film and electrical characteristics of a flexible $MoSe_2$

transistor under mechanical bending test.

Our multilayer $MoSe_2$ field-effect transistors exhibited high mobility (~ 121 $cm^2V^{-1}s^{-1}$), a high on/off current ratio (> 10^4), and good mechanical flexibility while bending down to radii of 5 mm. The experimental results can be understood remarkably well by classical long-channel MOSFET theory. The $MoSe_2$ films presented in this work are attractive for the fabrication of high-speed thin-film devices for flexible integrated circuits, especially for applications such as humanoid robotics, flexible OLED displays, and human-centric soft electronics. This paper was published in journal of 'Advanced Materials', which was selected as a cover image.

e. Real-time electrical detection of epidermal skin MoS_2 biosensor for point-of-care diagnostics

Toward point-of-care diagnostics, various approaches have been proposed and, in particular optical detection is preferred due to its relatively simple and rapid process. At the same time, FET-based biosensors have attracted great attention as they can provide highly sensitive and label-free detection. In this work, we present highly-sensitive point-of-care devices in an epidermal skin-type with system-level integration of flexible MoS_2 FET biosensor, read-out circuits, and light-emitting diode (LED) that allow real-time detection of prostate cancer antigen (PSA). Regardless of physical forms or mechanical stress conditions, our proposed high-performance MoS_2 biosensors can detect PSA concentration of 1 pg/ml without specific surface treatment for anti-PSA immobilization on the MoS_2 surface. Furthermore, current modulation induced by the binding process was stably maintained longer than 2~3 minutes. The demonstrated results indicate that flexible MoS_2–based FET biosensors have a great potential as point-of-care diagnostics of prostate cancer as well as other biomarkers. This manuscript was selected as a cover image of Nano Research (2017, volume 4).

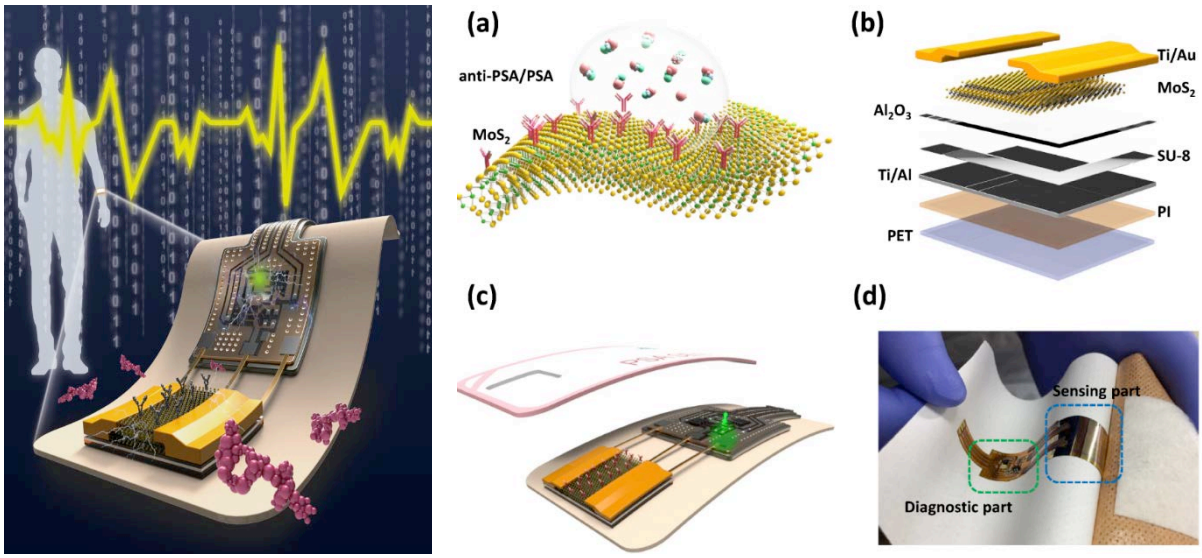

Figure 20: The cover image and an illustration and demonstration of platform of an epidermal skin-type MoS_2 biosensor system: (a) Schematic of a flexible MoS_2 biosensor detecting label-free immunoassay of PSA, where PSA antigen directly binds with PSA antibody functionalized MoS_2 surface. (b) Schematic layout of 2D multilayer MoS_2 FETs. c, d) Schematic illustration (c) and photograph (d) of an epidermal skin-type MoS_2 biosensor system, consisting of biosensor, read-out circuits, and LED as an indicator.

In a first demonstration, MoS_2 biosensors are designed to electrically detect PSA in a highly sensitive and label-free manner without the need of a chemically treated gate dielectric. The nature of hydrophobic MoS_2 surface (the contact angle ~ 75.77°) allows a physical adsorption to biomolecule binding, and doesn't require additional dielectric layers such as HfO_2 or SiO_2. Such an oxide-free operation can provide higher device sensitivity as well as a simpler device structure. Moreover, the use of "OFF" current for a transistor as an indicator strongly affords additional improvement in device sensitivity in MoS_2 biosensor and can compute the surface charge concentration due to anti-PSA/PSA binding quantitatively (Figs. 21(a) and 21(b)). Theoretical calculation of the MoS_2 biosensor operation provides a systematic understanding on the experimental demonstration of the MoS_2 biosensors in this study, and will open new pathways to fundamental studies of electrical 2D sensor applications for biological and chemical species.

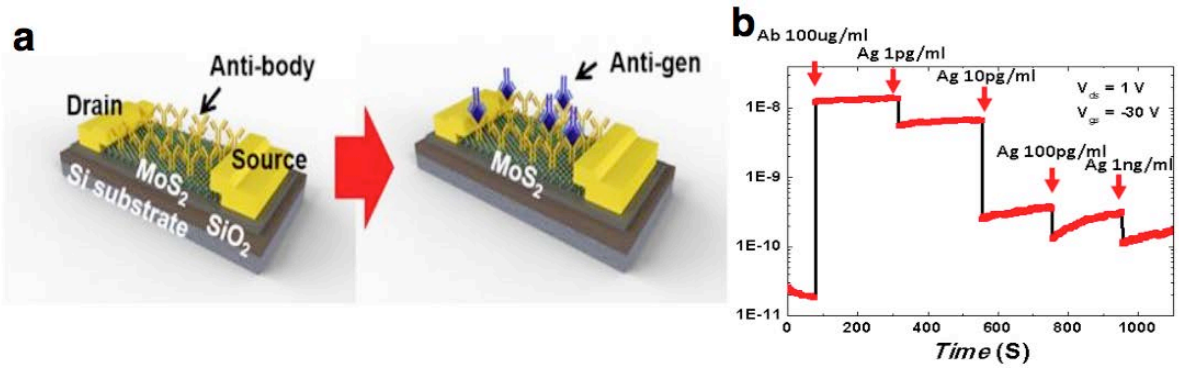

Figure 21: (a) Schematic of a MoS_2 biosensor configured as a PSA, detecting label-free immunoassay, illustrating PSA antibody functionalized MoS_2 surface (top) and subsequent binding of PSA antigen with antibody receptors. (b) Change of the off-current versus various PSA concentrations for an anti-PSA modified n-type MoS_2 transistor. As the concentration of PSA increases from 1 pg/mL to 10 ng/mL, the amount of selective binding of PSA to the anti-PSA immobilized MoS_2 nanosheet is approximately proportional to the PSA concentration.

List of Publications and Significant Collaborations that resulted from your AOARD supported project: In standard format showing authors, title, journal, issue, pages, and date, for each category list the following:

a) papers published in peer-reviewed journals,

1) Hyuk-Jun Kwon, Hongki Kang, Jaewon Jang, Sunkook Kim, and Costas P. Grigoropoulos, "Analysis of Flicker Noise in Two-dimensional Multilayer MoS_2 Transistors," *Applied Physics Letters*, 104, 083110 (2014).

2) Hyuk-Jun Kwon, Woong Choi, Daeho Lee, Yunsung Lee, Junyeon Kwon, Byungwook Yoo, Costas P. Grigoropoulos, and Sunkook Kim, "Selective and Localized Laser-Anneal Effect for High-Performance Flexible Multilayer MoS_2 Thin-Film Transistors," *Nano Research*, 7, 1137-1145 (2014).

3) Hyuk-Jun Kwon, Jaewon Jang, Sunkook Kim, Vivek Subramanian, and Costas P. Grigoropoulos, "Electrical Chracteristics for Multilayer MoS_2 Transistors at Real Operating Temperatures with Different Ambient Conditions," *Applied Physics Letters*, 105, 152105 (2014).

4) Seong Yeoul Kim, Seonyoung Park, and Woong Choi, "Variability of Ti Electrical Contact Properties in Multilayer MoS_2 Thin-Film Transistors," *Applied Physics A*, 117, 761 (2014).

5) Joonhyung Lee, Piyush Dak, Yeonsung Lee, Heekyeong Park, Woong Choi, Muhammad A. Alam, and Sunkook Kim, "Two-dimensional Layered MoS_2 Biosensors Enable Highly Sensitive Detection of Biomolecules," *Scientific Reports*, 4, 7352 (2014).

6) Jong Won Chung, Yeong Hwan Ko, Young Ki Hong, Wongeon Song, Chulseung Jung, Hoyoung Tang, Jiyoul Lee, Min hyung Lee, Bang-lin Lee, Yongwan Jin, Sangyoon Lee, Jae Su Yu, Jongsun Park, and Sunkook Kim, "Flexible Nano-Hybrid Inverter Based on Inkjet-printed Organic and 2D Multilayer MoS_2 Thin Film Transistor," *Organic Electronics*, 15, 3038-3042 (2014).

7) Yeonsung Lee, Jiyoul Lee, Ho Seok Park and Sunkook Kim, "Rendering High Charge Density of States in Ionic Liquid-Gated MoS_2 Transistors," *The Journal of Physical Chemistry C*, 118, 18278-18282 (2014).

8) Eun Hei Cho, Won Geun Song, Cheol-Joon Park, Jeongyong Kim, Sunkook Kim, and Jinsoo Joo, "Enhancement of Photoresponsive Electrical Characteristics of Multilayer MoS_2 Transistors using Rubrene-Patches," *Nano Research*, 8, 790-800 (2015).

9) Junyeon Kwon, Young Ki Hong, Hyuk-Jun Kwon, Yu Jin Park, Byoungwook Yoo, Jiwan Kim, Costas P. Grigoropoulos, Min Suk Oh, and Sunkook Kim, "Optically Transparent Thin-film Transistors based on 2D Multilayer MoS_2 and Indium Zinc Oxide Electrodes," *Nanotechnology*, 26, 035202 (2015).

10) Junyeon Kwon, Young Ki Hong, Gyuchull Han, Inturu Omkaram, Woong Choi, Youngki Yoon, and Sunkook Kim, "Giant Photoamplification in Indirect-Bandgap Multilayer MoS_2 Phototransistors with Local Bottom-Gate Structures," *Advanced Materials*, 27, 2224-2230 (2015).

11) Hyuk-Jun Kwon, Sunkook Kim, Jaewon Jang, and Costas P. Grigoropoulos, "Evaluation of Pulsed Laser Annealing for Flexible Multilayer MoS_2 Transistors," *Applied Physics Letters*, 106, 113111 (2015).

12) Junyeon Kwon, Seongin Hong, Young Ki Hong, Sungho Lee, Geonwook Yoo, Youngki Yoon, and Sunkook Kim, "Photosensitivity Enhancement in Hydrogenated Amorphous Silicon Thin-Film Phototransistors with Gate Underlap," *Applied Physics Letters*, 107, 201103 (2015).

13) Won Geun Song, Hyuk-Jun Kwon, Jozeph Park, Junyeob Yeo, Minjeong Kim, Suntak Park, Sungryul Yun, Ki-Uk Kyung, Costas P. Grigoropoulos, Young Ki Hong, and Sunkook Kim "High-Performance, Mechanically Flexible Multilayer MoS_2 Transistors with Highly Bending Stability," *Advanced Functional Materials*, 26, 2426-2434 (2016).

14) Young Ki Hong, Geonwook Yoo, Junyeon Kwon, Seongin Hong, Won Geun Song, Na Liu, Inturu Omkaram, Byungwook Yoo, Sanghyun Ju, Sunkook Kim, and Min Suk Oh "High Performance and Transparent Multilayer MoS_2 Transistors: Tuning Schottky Barrier Characteristics," *AIP Advances*, 6, 055026 (2016).

15) Hyuk-Jun Kwon, Jaewon Jang, and Costas P. Grigoropoulos, "Laser Direct Writing Process for Making Electrodes and High-k Sol-Gel ZrO_2 for Boosting Performances of MoS_2 Transistors," *ACS Applied Materials and Interfaces*, 8, 9314-9318 (2016).

16) Hyuk-Jun Kwon, Seungjun Chung, Jaewon Jang, and Costas P. Grigoropoulos, "Laser Direct Writing and Ink-Jet Printing for Sub-2μm Channel Length MoS_2 Transistor with High Resolution Electrodes," *Nanotechnology*, 27, 405301 (2016).

17) Jong-Soo Rhyee, Junyeon Kwon, Piyush Dak, Jin Hee Kim, Seung Min Kim, Jozeph Park, Young Ki Hong, Wongeon Song, Inturu Omkaram, Muhammad A. Alam, and Sunkook Kim, "High-Mobility Transistors Based on Large-Area and Highly Crystalline CVD-grown $MoSe_2$ Films on Insulating Substrates," *Advanced Materials*, 28, 2316-2321 (2016).

b) papers published in peer-reviewed conference proceedings,

1) Hyuk-Jun Kwon, Jaewon Jang, Hongki Kang, Sunkook Kim, Vivek Subramanian, and Costas P. Grigoropoulos, "Electrical Chracteristics for Multilayer MoS_2 Transistors at Real Operating Temperatures and Different Ambient Conditions," *ECS Transaction*, 64 (8) 127-133 (2014).

c) papers published in non-peer-reviewed journals and conference proceedings,

N/A

d) conference presentations without papers,

1) Seong Yeoul Kim, Seonyoung Park, and Woong Choi, "Variability of Contact Properties in MoS_2 Thin-Film Transistors," *International Meeting on Information Displays (IMID)*, August 26-29, Daegu, South Korea, 2014.

2) Young Ki Hong, Junyeon Kwon and Sunkook Kim, “Flexible 2D Multilayer MoS2 Electronics,” *AsiaNANO*, October 26-29, Jeju, South Korea, 2014

3) Sunkook kim, “Flexible 2D Layer Semiconducting Electronics,” *International Workshop on Flexible & Printable Electronics*, November 05-07, Chonju, South Korea, 2014.

4) Seong Yeoul Kim, Seonyoung Park, and Woong Choi, “Variability of Contact Properties in MoS_2 Thin-Film Transistors,” *International Conference Electronic Materials and Nanotechnology for Green Environment (ENGE)*, November 16-19, Jeju, South Korea, 2014.

5) Hyuk-Jun Kwon, Woong Choi, Sunkook Kim, and Costas P. Grigoropoulos, “Enhanced Performance of Multilayer MoS_2 Transistors with Picosecond Laser Annealed Contacts for Low Power Flexible Display,” *the 3rd International Education Forum on Environment and Energy Science (ACEEES)*, December 12-16, Perth, Australia, 2014.

6) Seong Yeoul Kim, Seonyoung Park, and Woong Choi, “Uncertainty of Contact Properties Between Ti and Naturally Occurring MoS_2,” *The 22nd Korean Conference on Semiconductors*, February 10-12, Incheon, South Korea, 2015.

7) Hyuk-Jun Kwon, Woong Choi, Min Suk Oh, Sunkook Kim, and Costas P Grigoropoulos, "Pulsed Laser Annealing for Advanced Performance of Mechanically Flexible and Optically Transparent Multilayer MoS_2 Transistors," *SPIE Optics + Photonics*, August 9-13, San Diego, USA, 2015.

7) Junyeon Kwon, Young Ki Hong, Gyuchull Han, Inturu Omkaram, Seonyoung Park, Woong Choi, Youngki Yoon, and Sunkook Kim, “Giant Photo-Amplification in 2D Multilayer MoS_2 Phototransistors,” *Materials Research Society (MRS) Spring Meeting,* April 6-10, San Francisco, USA, 2015.

8) Wongeun Song, Young Ki Hong, Minjung Kim, Jongyeol Baeck, Sungryul Yoon, Kiwook Kyung, and Sunkook Kim, “High Mobility 2D Multilayer MoS_2 Transistor for Flexible Electronics,” *Materials Research Society (MRS) Spring Meeting,* April 6-10, San Francisco, USA, 2015.

9) Seong Yeoul Kim, Seonyoung Park, and Woong Choi, “Variability of Electrical Contact Properties Between Ti and Naturally Occurring MoS_2 Semiconductors,” *Materials Research Society (MRS) Spring Meeting,* April 6-10, San Francisco, USA, 2015.

10) Seung Hyun Baek, Ilhyun Kim, Yura Choi, and Woong Choi, “Growth of centimeter-scale continuous MoS_2 monolayer by chemical vapor deposition,” *Materials Research Society (MRS) Spring Meeting,* April 6-10, San Francisco, USA, 2015.

e) manuscripts submitted but not yet published, and

1) Geonwook Yoo, Heekyeong Park, Minjung Kim, Jingon Lee, Won Geun Song, Seokhwan Jeong, Min Hyung Kim, Hyungbeen Lee, Sang Woo Lee, Young Ki Hong, Min Goo Lee, Sungho Lee, and Sunkook Kim, “Real-Time Electrical Detection of Epidermal

Skin MoS_2 Biosensor for Point-of-Care Diagnostics," *Nano Research,* Accepted (2017).
2) Jongyeol Baek, Demin Yin, Na Liu, Inturu Omkaram, Chulseung Jung, Healin Im, Seongin Hong, Seung Min Kim, Young Ki Hong, Jaehyun Hur, Youngki Yoon, and Sunkook Kim, "A Highly Sensitive Chemical Gas Detecting Transistor Based on Highly Crystalline CVD-grown $MoSe_2$ Films," *Nano Research,* Accepted (2017).

f) provide a list any interactions with industry or with Air Force Research Laboratory scientists or significant collaborations that resulted from this work.

The laser doping work at UC Berkeley transitioned to a project funded by Samsung since 9/1/15.

Attachments: Publications a), b) and c) listed above.